metals

Review

A Review of Friction Stir Processing of Structural Metallic Materials: Process, Properties, and Methods

Anna P. Zykova [1,*], Sergei Yu. Tarasov [1,2], Andrey V. Chumaevskiy [1] and Evgeniy A. Kolubaev [1]

[1] Institute of Strength Physics and Materials Science, Siberian Branch of Russian Academy of Sciences, 634055 Tomsk, Russia; tsy@ispms.ru (S.Y.T.); tch7av@gmail.com (A.V.C.); eak@ispms.ru (E.A.K.)

[2] Division for Materials Science, National Research Tomsk Polytechnic University; 634050 Tomsk, Russia

* Correspondence: zykovaap@mail.ru; Tel.: +7-(3822)28-68-63

Received: 22 May 2020; Accepted: 4 June 2020; Published: 9 June 2020

Abstract: Friction stir processing (FSP) has attracted much attention in the last decade and contributed significantly to the creation of functionally graded materials with both gradient structure and gradient mechanical properties. Subsurface gradient structures are formed in FSPed metallic materials due to ultrafine grained structure formation, surface modification and hardening with various reinforcing particles, fabrication of hybrid and in situ surfaces. This paper is a review of the latest achievements in FSP of non-ferrous metal alloys (aluminum, copper, titanium, and magnesium alloys). It describes the general formation mechanisms of subsurface gradient structures in metal alloys processed by FSP under various conditions. A summary of experimental data is given for the microstructure, mechanical, and tribological properties of non-ferrous metal alloys.

Keywords: friction stir processing; aluminum alloys; copper alloys; titanium alloys; magnesium alloys; subsurface gradient structures; surface modification; hardening with reinforcing particles; hybrid in situ surfaces

1. Introduction

Structural metal alloys have a long history of industrial applications and are still of great practical relevance for the manufacture of multifunctional products, components, and structures. These are aircraft fuselage and wing components, fuel and cryo tanks, rocket bodies, engine mounts, wheel disks, automobiles, aluminum bridges and pipelines, heat exchangers, air conditioners in construction engineering, railway car bodies, frames and bases of underground trains, and many others. The main feature of such components and structures is their long-term performance capabilities under given loads, which is largely determined by the choice of a suitable alloy to provide the desired properties. Along with the chemical composition of the alloy, the mechanical properties and performance of structures are also governed by an appropriately selected high-quality method of processing.

It is well known that the strength of metal parts can be improved by reinforcing them with alloying elements, metal fibers, or powders of various size and chemical composition [1–16]. This topic has been extensively studied since the 1980s. Over the past decade, much attention has been given to methods for the formation of subsurface gradient structures in metallic materials, such as plasma spraying [17–20], cold spraying [21–23], laser melting [24–26], ion implantation [27–32], and others. Unfortunately, the listed methods for the bulk and surface processing of metallic materials have many drawbacks, e.g., agglomeration of additive particles and their nonuniform distribution both in the bulk and on the surface of the alloy, formation of unwanted phases and interfacial reactions due to high processing temperatures, formation of numerous defects in ion implanted surface layers or formation of amorphous layers at high radiation doses, the need for thermal treatment or other additional processing methods, sophisticated processing equipment, low processing efficiency, and so on.

Friction stir processing technology is a good alternative to overcome the disadvantages mentioned above, because it is performed at temperatures below the melting temperature of base alloys [33–35]. This method is relatively new and is based on the physical principles of friction stir welding (FSW) [33]. Unlike FSW intended for joining together dissimilar solid materials, friction stir processing locally modifies the alloy microstructure to achieve the desired specific properties. It has clear advantages over other surface treatment methods for metallic materials:

(1) FSP is a solid-state, one-stage processing technique that provides grain refinement, strengthening, and structural homogeneity without changing the shape and size of the processed metallic material [33];
(2) the microstructure and mechanical properties of the processed parts can be easily controlled by varying the process parameters [33,35,36];
(3) the method is both environmentally friendly and energy efficient. FSP has greatly evolved over recent decades and have found many practical and scientific applications [33].

The growth of interest in FSP according to the Scopus database began in 2001 and continues to the present. In 2011–2015, the studies were mostly devoted to the surface processing of various metals and alloys. Since 2009 there has been increasing interest in the fabrication of particle-reinforced metal matrix composites, hybrid composites, and in situ composites on the basis of metals and alloys. Currently, the metallic materials produced by different FSP techniques can be conditionally classified into several main groups:

- materials with a subsurface gradient structure obtained through the formation of equiaxed nanograins and structural homogenization [37–57];
- materials with a compositional subsurface gradient structure formed by modifying and hardening the material surface with various reinforcements [32,58–77];
- in situ and hybrid composites [71,78–91].

The aim of this work is to review the latest progress in friction stir processing of non-ferrous metal alloys (aluminum, copper, titanium, magnesium alloys) in accordance with the proposed classification. We will discuss the mechanisms used in FSP for the formation of subsurface gradient structures under various conditions. Particular experimental results will be summarized to show the relationship between the FSP parameters and the resulting microstructure/mechanical properties.

2. Friction Stir Processing

2.1. Principles and Processes

The friction stir processing method evolved from the friction stir welding technology and involves similar processes and principles [92,93]. The friction-heated and plasticized metal is subjected to severe plastic deformation by stirring, which results in obtaining a homogeneous recrystallized fine-grained microstructure. The principle diagram of the FSP/FSW process is shown in Figure 1. The base metal (matrix) is mechanically stirred using a non-consumable rotating tool with a pin (Figure 1a). The tool rotates at a high rate and then is plunged into the workpiece under axial force until the tool shoulder contacts the workpiece surface. Then the tool is advanced over the workpiece along the processing direction. Friction between the tool and the workpiece produces a large amount of heat. As the temperature rises due to frictional heat, the base metal softens in the processing zone and undergoes severe plastic deformation while being entrained by the rotating and traversing pin. This is the basic principle of modifying metallic materials by FSP, resulting in the formation of a subsurface gradient structure in the material via grain refinement and microstructural homogenization. Some friction stir welding or processing techniques involve additional processes, e.g., application of ultrasound to the welding/processing zone (Figure 1c) [94] or multi-pass processing to harden the entire surface area (Figure 1b) [42].

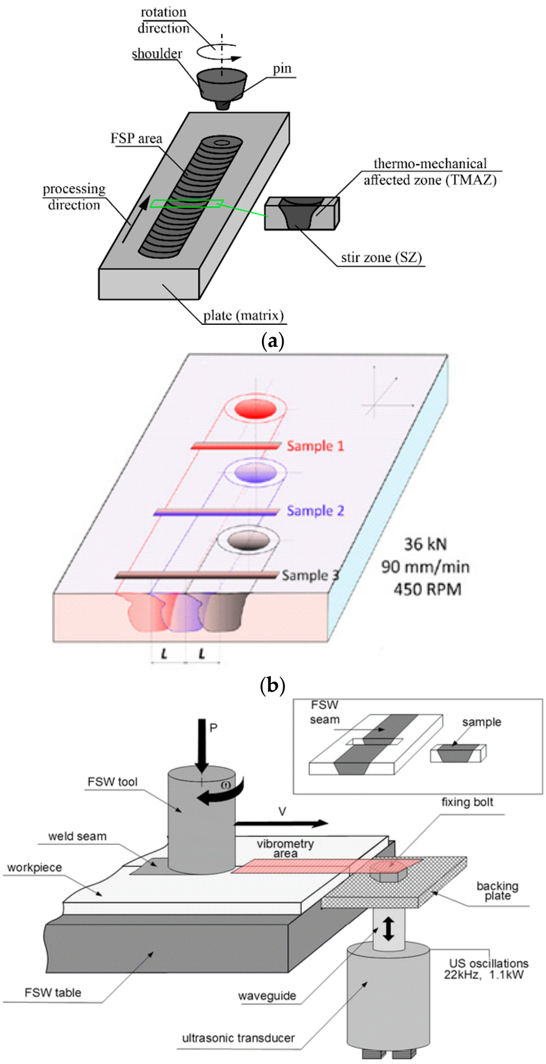

(**c**)

Figure 1. Schematic diagram of the FSP process: (**a**) multi-pass FSP process (**b**) (reproduced from [42], with permission from Springer, 2019) and FSW process with ultrasound assistance (**c**) (reproduced from [94], with permission from Springer, 2017).

2.2. FSP Process Parameters

The main FSP parameters are the tool rotation rate, traverse speed, tool tilt angle, pass time, tool geometry and size, and axial force on the tool.

The temperature in the processing zone during FSP ranges from 0.6 T_m to 0.9 T_m (where T_m is the metal melting temperature), and the strain rate is 1–10^{-3} s^{-1}. Together, they cause pronounced thermal effect, plastic deformation, and material stirring [36]. The most important parameters affecting the microstructure and mechanical properties of the processed material are the tool rotation rate, traverse speed, and axial force. By varying these parameters, FSP can be performed with different heat input conditions and material plastic flow regimes.

FSP allows healing the metal defects such as porosity, cracks, etc. and modifies the alloy microstructure by crushing large matrix grains, second phase particles, and dendrites in cast alloys. Similarly, FSP may crush and dissolve agglomerates of reinforcing particles introduced into metal matrix composites. In both cases, second phase or reinforcing particles are homogenized or uniformly distributed in the metal matrix. The structural homogenization and elimination of defects becomes more pronounced with either increasing rotational rate or decreasing traverse speed due to higher heat release, effective metal viscosity, and more intense flow of the plasticized material. At a lower rotational rate but higher traverse speed, the generated heat contributes to the grain refinement and corresponding metal strengthening [45,51]. A higher rotational rate but lower traverse speed lead, to less pin travel per revolution, producing larger amounts of heat, possibly resulting in grain coarsening and hardness deterioration [33,36,95]. A long-term thermal effect on the material can be favorable for in situ reactions because of the formation of larger amounts of hardening phases uniformly distributed in the matrix [86,96–99].

The microstructure and mechanical properties of metal alloys can also be modified by increasing the tool pass time, changing the tool rotation direction between the passes, or using multi-pass FSP; however, the results vary for different materials [42,44,45,47,93,100–104]. Multi-pass FSP is widely used to fabricate composites with a more homogeneous phase distribution than in single-pass FSPed materials as well as with more efficient in situ reactions during processing [78,86,87,105]. Multi-pass FSP is also used to obtain materials with a large processing area by making closely spaced tracks; the overlapping zone between two adjacent tracks exhibits a complex structure [42].

The tool size and the pin shape strongly influence the heat production and material flow during FSP [40,41,92,93]. At the very beginning of tool plunging, heating occurs mainly due to friction between the pin and the workpiece. Some additional heating results from material deformation. The tool is plunged into the workpiece until the shoulder contacts its surface. According to the studies on the role of pin geometry in heat generation at the plunge stage, the effective pin area has a direct effect on friction-induced deformation and heat production. This suggests that circular pins produce the lowest temperature during plunging [93]. The effect of the tool size and geometry on the microstructure and properties of materials is studied in detail in Refs. [36,40,41,92,93,106–108].

2.3. Microstructure in FSP

Microstructural changes in FSPed materials are caused by thermomechanical effects. As in the case of FSW, the FSP area has a stir zone (SZ), a thermomechanically affected zone (TMAZ), a heat affected zone (HAZ), and a base metal zone (BM) (Figure 2) [36,41,92]. The stir zone has a typical onion ring structure formed when layers of plasticized material flow in the direction from the advancing to the retreating side of the tool. The stir zone material is strongly heated in FSP due to friction and severe plastic deformation, leading to a dynamically recrystallized microstructure. That is why the stir zone consists mainly of uniform refined equiaxed grains much finer than those in the base metal [42]. The structure of these grains is in most cases characterized by a high proportion of high-angle boundaries [37,48,49,54,89,109,110]. FSP parameters such as the tool geometry, workpiece temperature, and axial pressure significantly affect the size of recrystallized grains in the stir zone.

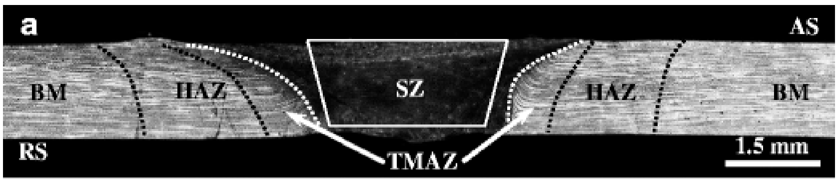

Figure 2. A typical macroimage of different microstructural zones in a FSWed material (reproduced from [94], with permission from Springer, 2017).

3. FSP Applications for Different Materials

3.1. FSP of Structural Alloys

Mechanical characteristics of crystalline structural materials are largely dependent on defects (porosity, shrinkage, cracks, etc.) and the coarse-grained structure of cast material. It is known that the strength of an alloy is enhanced by decreasing the grain size, according to the Hall-Petch equation [111]. To turn a coarse-grained alloy into a fine-grained crystalline material, the alloy can be subjected to severe plastic deformation in order to produce a high density of dislocations and then to rearrange these dislocations to form a grain boundary array. In friction stir processing of structural alloys, the material is heated up due to friction and severe plastic deformation, and as a result the stir zone is dynamically recrystallized. Givi and Asadi [112] proposed three types of dynamic recrystallization mechanism during FSP: (1) intermittent dynamic recrystallization occurring during the nucleation and growth of new grains; (2) continuous dynamic recrystallization involving the formation of low-angle boundary arrays and a gradual increase in boundary misorientation under hot deformation, which finally leads to the nucleation of new grains; and (3) geometric dynamic recrystallization resulting from collision with serrated grain boundaries formed when grains are highly elongated due to severe hot deformation. Thus, FSP forms a subsurface gradient structure with fine equiaxed recrystallized grains of uniform size, due to which the alloy strength and hardness increase. According to the literature data, FSP was applied to aluminum [37–44], copper [46,48–50,107,110], titanium [51–55,113], magnesium alloys [56,57], steels [114–119] and high-entropy alloys [120–125]. The FSP efficiency depends on the tool rotation rate, traverse speed and the number of passes, and is determined for each type of alloy differently. It was shown below for light structural alloys basing on Al, Cu, Ti, Mg.

3.2. *FSP of Aluminum Alloys*

A review of experimental studies shows that single-pass FSP with low tool rotation rates may reduce the average grain size in aluminum alloys by 85–96%. Figure 3 illustrates a typical macro- and microstructure of aluminum alloys before and after FSP.

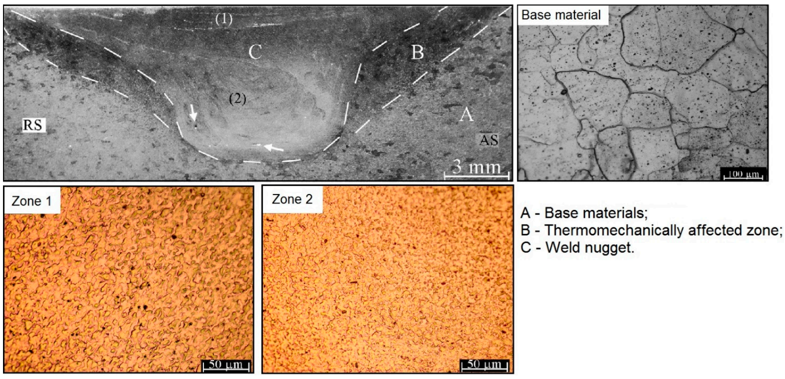

Figure 3. Macro- and microstructure of single-pass FSPed 6063 aluminum alloy (reproduced from [39], with permission from Elsevier, 2019).

By way of example, Table 1 gives the experimental data for FSPed aluminum alloys, showing the effect of FSP on the grain structure and strength of the alloys. The choice of parameters such as the number of FSP passes, tool rotation rate, and traverse speed depends on the aluminum alloy grade and leads to ambiguous results.

A study of single- and multi-pass FSPed A356 aluminum alloy [37] revealed that an increase in the number of passes leads to porosity elimination, refinement of primary silicon particles (from 188 to 2.5–1.6 μm) and α-Al grains (up to 0.4–0.51 μm), as well as to higher hardness. The α-Al grains demonstrate mainly high-angle boundaries and various stages of recovered substructures and dislocation densities. The first FSP pass may produce subgrains and low-angle boundaries by migration of dislocations. During the second and third passes, the formed second phase particles impede the grain boundary migration and thereby limit the recrystallization front, leading to the formation of submicron grains [37]. After six passes, second phase particles are coarsened and cannot provide a sufficient Zener pinning-type effect. That is why no noticeable refinement of subgrains was observed compared to other passes [37]. Similar results were obtained in Ref. [38] (Table 1).

Table 1. Experimental data on FSP of aluminum alloys.

Material	Tool Rotation Rate, rpm	Traverse Speed, mm/min	Number of Passes	Average grain size of the Base Alloy/Average Grain Size after FSP, μm	Mechanical Properties	Ref. No.
A356	350	16	1	-/0.74	MH: 68 HV	[37]
			2	-/0.58	MH: 92 HV	
			3	-/0.45	MH: 113 HV	
			6	-/0.51	MH: 133 HV	
Al-12Si	1400	28	1	25/-	MH: ↑ 20.9% UTS: ↑ 15.1% Elong.: ↑ 3.7 times	[38]
Al5052	1120	80	1	243/16.5	MH: ↑ 13.3%	[59]
AA5005-H34	490	127	1	-/10.7	MH: 42.6 HV UTS: 135.3 MPa Elong.: 34.4%	[40]
	970			-/18.5	MH: 38.9 HV UTS: 118.7 MPa Elong.: 37.3%	
	1200			-/20.4	MH: 37.9 HV UTS: 119.3 MPa Elong.: 41.4%	
6063	300		1	134/5.3	UTS: ↓ 6% Elong.: ↓ 42%	[39]
			2	134/8.6	UTS: ↓ 21% Elong.: ↓ 40%	
	500		1	134/5.5	UTS: no change Elong.: ↓ 28%	
			2	134/9.6	UTS: ↓ 10% Elong.: ↓ 29%	
	700		1	134/7.5	UTS: ↑ 15% Elong.: ↓ 36%	
			2	134/9.7	UTS: ↑ 5% Elong.: ↓ 36%	
	1000		1	134/8	-	
	1200		1	134/7.8	-	

Table 1. *Cont.*

Material	Tool Rotation Rate, rpm	Traverse Speed, mm/min	Number of Passes	Average grain size of the Base Alloy/Average Grain Size after FSP, µm	Mechanical Properties	Ref. No.
5086	1025	30	1	48/7	MH: ↑ 8.6% UTS: ↑ 3.8% Elong.: ↑ 30.7%	[43]
		80		48/10.5	MH: ↑ 8.6% UTS: ↑ 9.6% Elong.: ↑ 23%	
		150		48/3.8	MH: ↑ 10% UTS: ↑ 1.9% Elong.: ↑ 19.2%	
		30	12 (intermittent)	48/8	MH: ↑ 6.9% UTS: ↑ 5.7% Elong.: ↑ 40.3%	
		80		48/13.5	MH: ↑ 5.7% UTS: ↓ 19.2% Elong.: ↑ 19.2%	
		150		48/4	MH: ↑ 5.6% UTS: ↓ 3.8% Elong.: ↑ 15.3%	
		30	12 (continuous)	48/10.5	MH: ↓ 4.3% UTS: ↑ 1.9% Elong.: ↑ 32.7%	
		80		48/15	MH: ↑ 1.4% UTS: ↓ 30.8% Elong.: ↑ 3.8%	
		150		48/6	MH: ↑ 4.3% UTS: no change Elong.: ↑ 7.6%	
AA1050	1600	20	1	42.85/10.58	MH: ↑ 47.6% CF: ↓ 13.8%	[62]

A higher tool rotation rate may serve to increase the mean grain size and reduce the strength. Zhao et al. [39] who studied the influence of the tool rotation rate ranging from 300 to 1200 rpm and showed a 16–26-fold reduction in the mean grain size in the stir zones of single- and multi-pass FSPed 6063 aluminum alloy. As the tool rotation rate increased from 300 to 1200 rpm, the grain size increased from ~5 to ~8 µm and from ~8.5 to ~9.7 µm after one and two passes, respectively [39]. However, despite the significant grain refinement after FSP, some mechanical properties deteriorated in comparison with those of the base alloy (Table 1). This is explained by the fact that the base material contains a high density of needle-shaped precipitates, the amount of which decreases after FSP, or the precipitates undergo strain-induced dissolution at high temperature during processing. The reduced density of needle-shaped fine precipitates in the stir zone is the reason for its lower mechanical properties than those of the base material. Similar results were reported in Ref. [40]. Another study by Ramesh et al. [43] performed on 5086 aluminum alloy subjected to discontinuous and continuous single- and twelve-pass FSP at a constant rotation rate of 1025 rpm but varying traverse speed (30–150 mm/min) revealed a growth of the mean grain size and a corresponding decrease in strength. It was shown that the best structure and properties of the alloy are achieved in single- and multi-pass FSP with the traverse speed of 30 mm/min. With further increasing traverse speed, the average grain size first increases and then decreases, the ductility is enhanced, and the strength of 5086 alloy is reduced (Table 1).

3.3. FSP of Copper Alloys

Pure copper is widely used in optical and electronic applications owing to its high electrical conductivity, thermal conductivity, and corrosion resistance. High purity copper alloys have low strength and wear resistance; therefore they are not popular in applications that require high strength properties. FSPed copper alloys (Cu 99.9%) demonstrate high ductility (up to δ = 70%) and relatively high strength (up to σ_B = 330 MPa), because their average grain size is reduced by about 51–99% when varying FSP parameters and performing additional passes [46–49,110]. The effect of FSP on pure copper was investigated using various tool pin geometries (plain cylindrical, threaded cylindrical, triflute, triangle, square, and hexagonal) [107,126] with fixed rotational rate and traverse speed to provide low heat input. The tool with the threaded cylindrical pin profile was found to be more effective in bringing about the desired mechanical modification of pure copper than other pin profiles used under low heat input conditions [107].

A typical macro- and microstructure of FSPed copper alloy is presented in Figure 4. As one can see, the macrostructure of the processed area exhibits the typical zones described in Section 2.3. Table 2 lists the properties of copper alloy samples, indicating the presence of fine equiaxed grains with a large fraction of high-angle boundaries which contribute to higher strength of copper alloys.

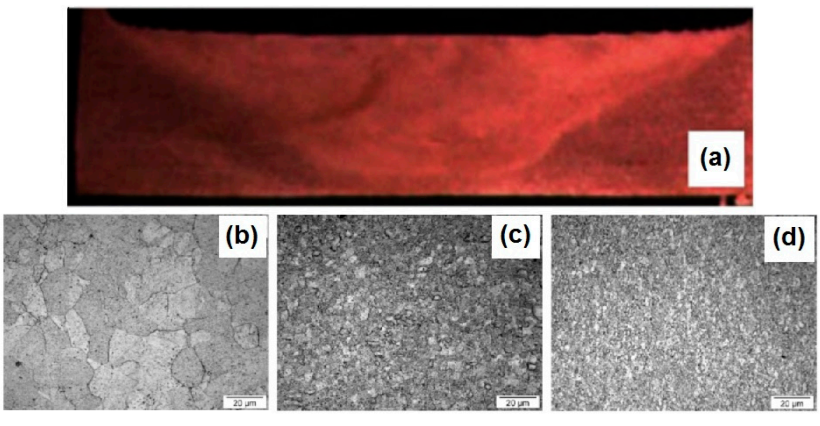

Figure 4. Optical images of single-pass FSPed copper alloy (reproduced from [47], with permission from Elsevier, 2011) (**a**) macrostructure; (**b**) base material; (**c**) nugget regions of specimens processed at 50 and (**d**) 250 mm/min.

Table 2. Experimental data on FSP of copper alloys.

Material	Tool Rotation Rate, rpm	Traverse Speed, mm/min	Number of Passes	Average Grain Size of the Base Alloy/Average Grain Size after FSP, μm	Mechanical Properties	Ref. No.
Cu (99.86%)	300	50	1	19/9.3	MH: ↑ 20% UTS: ↑ 18.1% Elong.: ↑ 9%	[47]
		100	1	19/6.1	MH: ↑ 21% UTS: ↑ 19.2% Elong.: ↑ 4.5%	
		150	1	19/5.9	MH: ↑ 32% UTS: ↑ 19.6% Elong.: ↑ 4.5%	
		200	1	19/3.6	MH: ↑ 33% UTS: ↑ 19.6% Elong.: ↑ 4.5%	
		250	1	19/3.0	MH: ↑ 34% UTS: ↑ 21.4% Elong.: ↑ 4.5%	
Cu (99.99%)	630	40	1	50–60/7.5	UTS: ↑ 30% Elong.: ↑ 2.9 times	[110]
			4	50–60/0.7–0.8	UTS: ↑ 43.3% Elong.: ↑ 1.8 times	
	630	315	1	50–60/2.5	UTS: ↑ 43.3% Elong.: ↑ 2.4 times	
			4	50–60/4–5	UTS: ↑ 43.3% Elong.: ↑ 2.4 times	
	1600	40	1	50–60/6	UTS: ↑ 46.7% Elong.: ↑ 3.9 times	
			4	50–60/2	UTS: ↑ 33.3% Elong.: ↑ 4.2 times	
Cu (99.95%)	400 600 800 1200	20	1	15/0.156 15/0.265 15/0.126 15/0.109	-	[48]

Table 2. *Cont.*

Material	Tool Rotation Rate, rpm	Traverse Speed, mm/min	Number of Passes	Average Grain Size of the Base Alloy/Average Grain Size after FSP, μm	Mechanical Properties	Ref. No.
Cu (99.98%)	250	50	1	35/5-20	MH: ↑ 18.2% UTS: - Elong.: -	[49]
	350				MH: ↑ 13.4% UTS: ↓ 18.2% Elong.: ↓ 1.7 times	
	500				MH: ↑ 7.3% UTS: ↓ 17.9% Elong.: ↑ 1.4 times	
Cu-0.18wt%Zr	600	50	1	40.5/9.7	-	[50]
		100		40.5/6.6		
		150		40.5/4.9		
		200		40.5/4.6		

Analysis of experimental data shows that FSP of copper alloys (Cu 99.9%) is efficient under low heat input conditions, and the efficiency increases with increasing traverse speed. For example, Surekha and Els-Botes [47] synthesized a high strength and high-conductivity copper using FSP with low heat input by varying the traverse speed from 50 to 250 mm/min (Figure 4) at a constant rotational rate of 300 rpm. By increasing the traverse speed from 50 to 250 mm/min, they refined the grains in the stir zone from 9 to 3 μm and simultaneously increased the hardness from 102 to 114 HV [47]. The grain refinement achieved at a constant rotational rate but increased traverse speed led to the improvement of mechanical characteristics, according to the Hall–Petch relationship [47]. Similar results were obtained in Refs. [50,110]. Barmouz et al. [45] investigated single-pass FSP on a pure copper plate by applying the traverse speeds of 40 and 315 mm/min while keeping the tool rotation rate at 630 rpm. FSP at higher traverse speed resulted in higher strength as demonstrated in Table 2. Four-pass FSPed specimens of the same material had an ultrafine-grained structure with a mean grain size of up to 800 nm [45].

Using higher tool rotation rate during copper alloy processing may cause the formation of both ultrafine and nano-sized grains with high-angle boundaries [48,49,110], as well as consequent improvement of the tensile strength [110]. Cartigueyen et al. [49] studied the effect of the FSP heat release on the mechanical properties of FSPed copper. The results showed that the temperatures reached during FSP strongly affected the microstructure and properties of the processed copper. It was found that the peak temperatures for the characteristic FSP zones range between 320 °C and 445 °C (about 0.3–0.42 T_m), indicating the achievement of low heat input conditions. The peak temperatures were higher on the advancing side of the FSP track as compared to those in the middle of the stir zone and on the retreating side. A fine and homogeneous grain structure was produced with various FSP tool rotation rates (Table 2). The authors observed the formation of a tunnel defect at 250 rpm, which was caused by insufficient heat input and significantly impaired the mechanical properties of the processed metal. The hardness of the FSPed copper was strongly dependent on the tool rotation rate (Table 2). The minimum rotational rate for performing efficient FSP under low heat input conditions was found to be equal to 350 rpm [49].

3.4. FSP of Titanium Alloys

Titanium and its alloys are widely used in aerospace, chemical, and biomedical industries due to high specific strength, corrosion resistance, and good biocompatibility. Biomedical and aerospace applications often require only surface hardening of titanium alloy products, while retaining its original structure and composition in the bulk. Since the surface layer hardness determines the wear resistance, surface hardening is performed to improve the surface of soft pure titanium. FSP can be used to increase the sliding wear resistance and surface hardness of alloys by changing the surface microstructural characteristics such as grain refinement and strain hardening [51–54]. However, the issue of wear resistance is too complex and cannot be reduced only to increasing the hardness. As far as nanostructured metals are concerned, there is no unambiguous opinion on whether their wear resistance is higher or lower as compared to that of coarse-grained ones. Many nanostructured metals and alloys lose their ductility and therefore become prone to subsurface fracture during sliding friction. Also, the abundance of grain boundaries adds to a higher amount of dangling bonds and therefore, a higher probability of adhesion bonding to the counter body. Zhang et al. [54] produced an ultrafine microstructure in FSPed Ti-6Al-4V alloy, which consisted of α grains (~0.51 μm) and a small amount of β-phase with a high fraction of high-angle grain boundaries (89.3%). Mironov et al. [52] found that the stress state in FSPed pure titanium is close to simple shear, where the shear plane resembles a truncated cone with a diameter close to the tool shoulder diameter in the upper part of the stir zone and close to the pin diameter in its lower part. The authors [52] demonstrated that the material flow arises mainly from the prism slip and leads to a pronounced P-fiber {hkil} $\left\langle 11\bar{2}0 \right\rangle$ shear texture in the stir zone. The texture evolution governs the development of deformation-induced grain boundaries in this zone. The macro- and microstructure of pure Ti after single-pass FSP is shown in Figure 5 [51]. Table 3 gives the experimental data on the properties of FSPed titanium alloys.

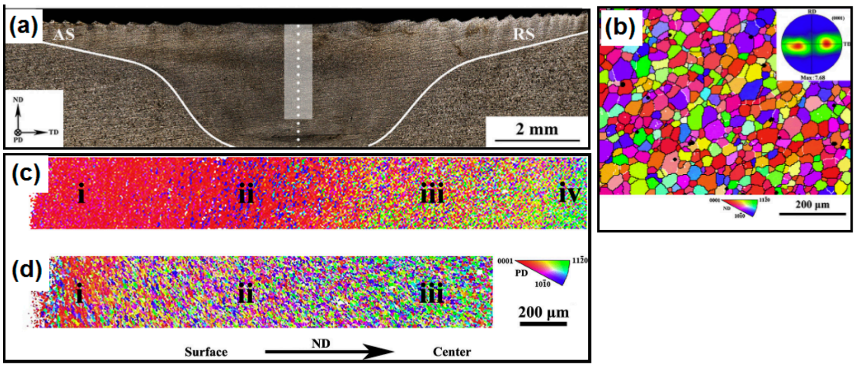

Figure 5. Macrostructure of single-pass FSPed titanium (reproduced from [51], with permission from Elsevier, 2019): (**a**) region processed at 180 rpm; (**b**) EBSD map of pure titanium sheet; EBSD maps of the specimen cross sections processed at 180 rpm (**c**) and 270 rpm (**d**).

Table 3. Experimental data on FSP of titanium alloys.

Material	Tool Rotation Rate, rpm	Traverse Speed, mm/min	Number of Passes	Average Grain Size of the Base Alloy/Average Grain Size after FSP, µm	Mechanical Properties	Ref. No.
α-Ti (99.6%)	180	25	1	33.1/5.8	MH: ↑ 27% YS: ↑ 71.7% UTS: ↑ 35.1%	[51]
α-Ti (99.85%)	250 300 350	75	1	42/7	MH: ↑ 18.4% UTS: 382–384 MPa	[53]
Ti-6Al-4V	120	30	1	-/0.51	-	[54]
Ti grade 2	1400	14	1 2 3	-	MH: ↑ 15% FC: ↓ 31% MH: ↑ 34.6% FC: ↓ 66% MH: ↑ 55.4% FC: ↓ 88.8%	[55]

Efficient FSP of pure titanium can be performed at both high (> 250 rpm) [53,55] and low tool rotation rates (< 250 rpm) [43]. At 180 rpm, the grain size in the stir zone decreases by 82% (from 33.1 to 5.8 µm), the microhardness increases by 27%, and the yield strength increases by 71.7% [51].

A study of the multi-pass FSP effect on the assessment of the microstructure and wear resistance of pure titanium showed that higher wear resistance and microhardness of specimens after 3 passes correlate with a smaller grain size [55] (Table 3).

3.5. FSP of Magnesium Alloys

The attractive properties of magnesium and its alloys include reduced weight, electromagnetic shielding, high specific strength, and so on. However, the alloys have limited formability, especially at ambient temperature, which significantly limits their industrial application. It is believed that grain refinement and texture weakening are effective ways to improve the ductility of magnesium. This can be achieved by FSP that can change the alloy microstructure and thus significantly increase its ductility without the tensile strength loss [127–129]. Typical macro- and microstructures of a magnesium alloy before and after FSP are shown in Figure 6. The experimental data on friction stir processing of particle-reinforced structural magnesium alloys are analyzed in Table 4.

Table 4. Experimental data on FSP of magnesium alloys.

Material	Tool Rotation Rate, rpm	Traverse Speed, mm/min	Number of Passes	Average Grain Size of the Base Alloy/Average Grain Size after FSP, μm	Mechanical Properties	Ref. No.
Al-Cu-Mg	450	-	1	137 × 22.2/9.1 × 6.4	MH: ↑ 15% UTS: ↑ 9%	[56]
AZ31	200	50	1	-/-	UTS: ↑ 4% Elong.: ↑ 9.5%	[129]
Mg-6Zn-1Y-0.5Zr	800	20	1	-/3.20	UTS: ↑ 32.6% Elong.: ↑ 146.7%	[128]
		80	1	-/2.37	UTS: ↑ 37.7% Elong.: ↑ 183.4%	
		200	1	-/1.65	UTS: ↑ 53% Elong.: ↑ 151.4%	
AZ31	400	50	1	16–300/6.6–3.5	MH: ↑ 22.2% UTS: ↑ 2 times Elong.: ↑ 1.5 times	[127]
AZ31	600 600 600 800 800 800	20 30 40 20 30 40	1	-/-	MH: ↑ 17.8% MH: ↑ 24.3% MH: ↑ 38% MH: ↑ 44.6% MH: ↑ 48.7% MH: ↑ 53.7%	[113]
AZ61	1000	37	2	75/0.04–0.2	MH: ↑ 3 times	[130]
AZ80	375	118	1 (in air)	-/7.1	MH: 69.4 HV	[131]
			1 (under water)	-/2.7	MH: 75.3 HV	
AE42	950	75	1	81/7.4	MH: ↓ 19.1% UTS: ↑ 22.9% Elong.: ↑ 2.7 times	[132]
QE22	800	100	1	38/0.88	UTS: ↓ 13.5% Elong.: ↑ 3 times	[133]
	800 600	100 100	1 2	38/0.63	UTS: ↓ 1.9% Elong.: ↑ 3.4 times	
	800 600	100 100	1 2	38/2.30	UTS: ↓ 30.7% Elong.: ↑ 1.7 times	

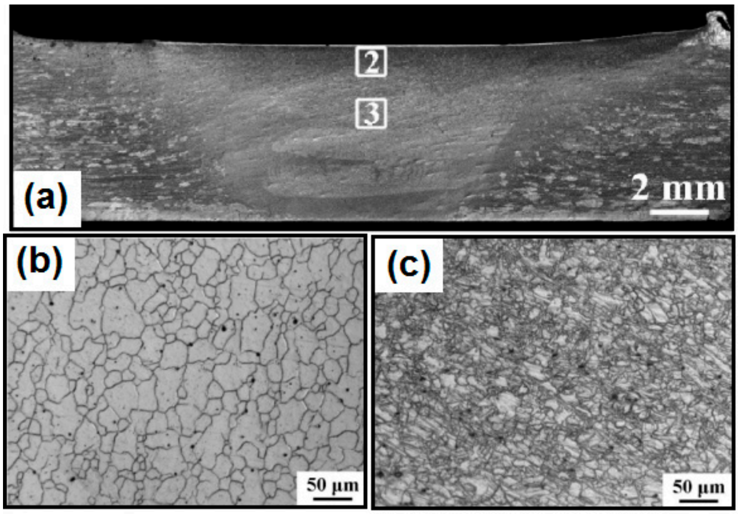

Figure 6. Macro- and microstructure of single-pass FSPed AZ31 alloy (reproduced from [129], with permission from Elsevier, 2019): (**a**) specimen macrostructure in the region processed at 200 rpm; (**b**) base alloy microstructure; (**c**) stir zone microstructure (2).

According to Wang et al. [128], FSP of a Mg-6Zn-1Y-0.5Zr casting resulted in dissolution and dispersion of the intergranular eutectic I-phase (Mg_3Zn_6Y). Hot deformation by FSP led to $I \rightarrow W$ ($Mg_3Zn_3Y_2$) phase transformation. An increase in the traverse speed caused significant grain refinement and the formation of a large fraction of fine particles, which greatly improved the yield strength (93.1%), tensile strength (53.0%), and relative elongation (151.4%) in comparison with those of the cast material [128].

A change in the phase composition after FSP was also observed in the cast alloy AE42 [132]. The β-$Mg_{17}Al_{12}$ and $Al_{11}RE_3$ phases dissolved after single-pass FSP, with the formation of a new Al_2RE phase. The factors affecting the strength of the cast magnesium alloy AE42 were found to be secondary phases (most influential), texture, and grain size [132].

As reported by Du and Wu [130] for AZ61 Mg alloy, a nano-grained structure can be produced by double-pass FSP under the condition of rapid heat removal by means of using an additional liquid nitrogen cooling system. The proposed processing technique allows reducing the mean grain size to <100 nm, thus increasing the alloy microhardness to 155 HV. The authors described the nanostructure evolution process as follows: (1) in the first FSP pass, submicron-sized grains are formed in the processed sheet by continuous dynamic recrystallization; (2) in the second pass, numerous nuclei are formed by discontinuous dynamic recrystallization due to the presence of submicron-sized grains, subgrains, and a high density of dislocation walls; (3) the growth of recrystallized grains is limited by effective liquid nitrogen cooling. Similar effects of remarkable grain structure refinement and improvement of mechanical properties by the above scenario are described in Refs. [128,132,133].

4. Friction Stir Processing of Particle-Reinforced Structural Alloys

The last decade showed a growing interest in friction stir processing of particle-reinforced metallic materials. Such materials are referred to in the literature as metal matrix composites [59,60,63,71], composite materials [58,61,66], hybrid composites [69,73–75], and others. This processing method is used for fabricating surface composite coatings with an average thickness from 50 to 600 μm on the basis of aluminum, copper, titanium, and magnesium alloys. The reinforcing additives for the surface composites can be in the form of powder, fibers, or platelets, which are most commonly filled into especially milled grooves [59,61,63–65,69,73,78,80,81,86,93] or drilled holes [69,73–75] (Figure 7). A typical subsurface macro- and microstructure of the stir zone with introduced particles is shown in Figure 8.

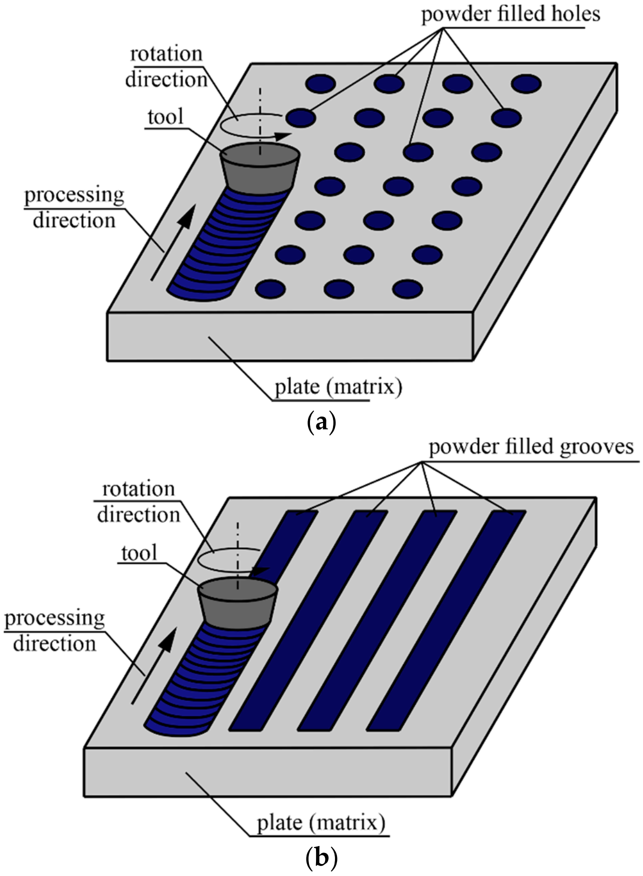

Figure 7. Schematic of the FSP process with the addition of reinforcements filled (**a**) into holes in the substrate and (**b**) into a groove.

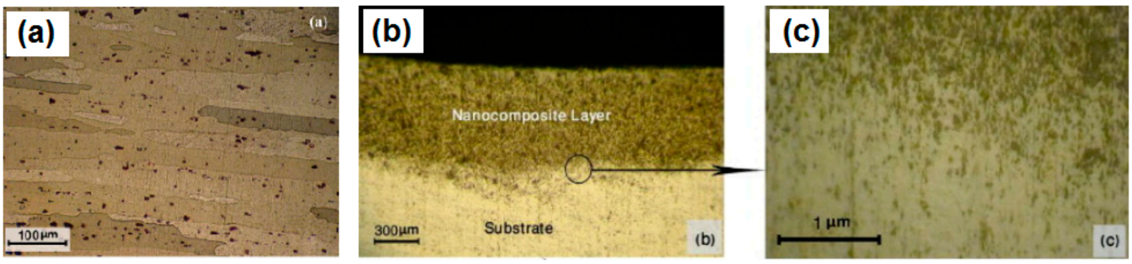

Figure 8. Microstructure of Al2024 (reproduced from [65], with permission from Elsevier, 2010): (**a**) microstructure of the base Al2024; (**b**) cross-sectional microstructure with Al_2O_3 particles after single-pass FSP; (**c**) interfacial microstructure with Al_2O_3 particles.

Hard fine-grained particles can be admixed to the substrate during FSP by the following mechanism. The heat generated by the friction of the tool shoulder and the pin plasticizes the metal matrix around and under the tool. Its rotational and translational motion entrains the plasticized metal matrix material from the advancing side to the retreating side. The flow of the matrix material breaks the grooves (or holes) and admixes the compacted particles to the plasticized metal matrix material. The tool rotation rate and traverse speed determine the stirring intensity and provide the formation of a composite. Analysis of experimental data shows that all types of reinforcing particles can be stirred with the plasticized metal matrix to form a composite. This fact is clearly demonstrated by Dinaharan et al. [71] who synthesized copper matrix composite layers reinforced with various ceramic particles. The authors showed that the type of ceramic particles does not affect the particle distribution pattern in the composite. Neither the density gradient nor the wettability of ceramic particles by the copper matrix lead to a nonuniform particle distribution. It is also noted that merging of the material flows caused separately by the tool shoulder and the pin leads to the formation of layers with a high and low volume fraction of ceramic particles due to the temperature gradient along the depth of the plate. The tool penetration depth is not equal to the total plate thickness in FSP. The absence of "onion rings" indicates that the temperature gradient along the pin penetration depth is negligible [71].

Severe plastic deformation and dynamic recrystallization during FSP result in a fine equiaxed grain microstructure in the stir zone, in which reinforcing particles are located both inside the grains and at the grain boundaries [61,63,71,76]. When introducing reinforcement particles into the matrix by FSP, no interfacial reactions were observed; there is a distinct boundary between the matrix and the introduced particles, e.g., as shown in Figure 9 for AA6063 alloy FSPed with the addition of vanadium particles [63]. The composite image in Figure 9 demonstrates a sharp boundary between the vanadium particles and the aluminum matrix. In Figure 9b, there are no reaction layers that would show contrast other than those of the matrix and the particle. This is confirmed by the EDX line scan (see inset in Figure 9b) indicating a sharp change in EDX counts in the narrow transition zone at the particle-matrix interface.

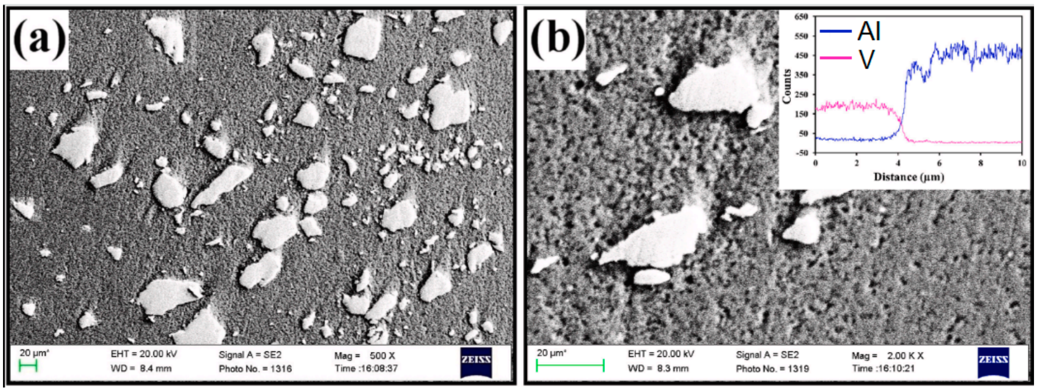

Figure 9. Microstructure of FSPed AA6063 with 12 vol. % V content at magnification: (**a**) 500× and (**b**) 2000× (the insert shows the EDX line scan along the particle interface) (reproduced from [63], with permission from Elsevier, 2019).

However, as noted in Refs. [59,62,64], the single-pass FSPed particle-reinforced alloy surface layers exhibit heterogeneous grain structure, nonuniform particle distribution and tensile properties. Multi-pass FSP allows producing a composite with more homogeneous particle distribution and grain structure, and with better tensile strength (Table 5) [59,62,64,68,70,72]. The mechanical and performance characteristics of composite metallic materials are also greatly affected by the content/volume fraction of the particles introduced. As shown for cast aluminum alloy A356 with a dendritic structure and a small number of pores [61], its processing with the addition of different volume fractions of Ti_3AlC_2 causes considerable elimination of coarse needle-like silicon particles and large primary aluminum dendrites, and produces a uniform distribution of fine Si and Ti_3AlC_2 particles in the matrix. A356 and Ti_3AlC_2 do not react during FSP, because the process time and temperature are too low to initiate mechanochemical or diffusion-controlled phase transformations. After FSP and an increase in the Ti_3AlC_2 particle volume fraction from 2.5 vol. % to 7 vol. %, tensile tests revealed a 2-fold increase in microhardness and mechanical properties (Table 5) [61]. A 3-fold improvement of the mechanical characteristics with increasing volume fraction of reinforcement particles during FSP was observed in Refs. [68,76]. Surface composites with different volume fractions of reinforcing particles (25 vol. % B_4C-75 vol. % TiB_2, 50 vol. % B_4C-50 vol. % TiB_2, and 75 vol. % B_4C-25 vol. % TiB_2) were synthesized by FSP in AA7005 alloy by Pol et al. [70]. They found that the hardness of the base alloy and Al7005-25 vol. % TiB_2-75 vol. % B_4C composite were 90 HV and 150 HV, respectively. The microhardness of surface composites with different volume fractions of the introduced particles were almost the same, which might be due to the same powder particle sizes. The synthesized surface composites of aluminum alloys demonstrated better ballistic resistance. The penetration depth of a steel projectile into the base alloy and composites 25 vol. % B_4C-75 vol. % TiB_2, 50 vol. % B_4C-50 vol. % TiB_2, and 75 vol. % B_4C-25 vol. % TiB_2 was 37 mm, 26 mm, 24 mm, and 20 mm, respectively, which is explained by the presence of hard reinforcing ceramic particles in the surface composite and by a hard core of the matrix [70].

Of particular interest are carbon materials (graphene, SWCNTs, MWCNTs, fibers, etc.) as high strength (30 GPa) reinforcement agents [67,68,134,135] for next-generation automotive and aerospace materials. S. Zhang et al. [68] demonstrated the microstructure and mechanical properties of nanocomposites are closely related to the energy input. In the cited work, different energy inputs led to different dispersion of CNTs in a CNTs/Al nanocomposite. Better CNT dispersion and higher tensile strength of a CNTs/Al nanocomposite was obtained at higher energy input (Table 5). The highest energy input led to a 53.8% higher maximum tensile strength of the nanocomposite than that of unreinforced aluminum. Moreover, nanocomposites showed a good improvement of ductility from 25% to 33% [68].

For an AA6061-graphene-TiB2 hybrid nanocomposite synthesized by Nazari et al. [69], it was shown that the simultaneous addition of graphene and TiB_2 particles during FSP led to a significant grain structure refinement in the stir zone; the average grain size was reduced to < 1 μm. Both graphene and TiB_2 particles retained their structure while being high-speed stirred into the aluminum alloy matrix. The hardness of the aluminum alloy increased to ~102 HV, mainly at the cost of TiB_2 particles introduced together with graphene with an optimal hybrid ratio of 1 wt. % graphene-20 wt. % TiB_2 [69]. With the same ratio of components, the processed hybrid nanocomposites demonstrated the best combination of tensile properties, namely three times higher yield strength and ~70% higher ultimate tensile strength (Table 5) [69].

There are also experiments on the fabrication and single-/multi-pass FSP of cast metal matrix composites [75,108,136]. The FSPed cast metal matrix composites exhibit a gradient structure represented by the bulk-reinforced matrix and the FSP-hardened surface layers. Arokiasamy and Ronald [75] described the process of stir casting a magnesium-based hybrid composite at the melting temperature of 700 °C with the introduction of SiC and Al_2O_3. It was shown that additional FSP of the cast composite increases its microhardness by 17.5%. Single-pass FSP led to a considerable grain refinement in the cast magnesium composite (Table 5). Microstructural studies revealed uniform distribution of SiC and Al_2O_3 particles both in the bulk of the material and in the stir zone [75].

Hardening of composite aluminum alloy surfaces by FSP is performed using fine powders of the following chemical composition: Al6061-SiO_2 [58], Al-Al_2O_3 [64,65], AA6016-(Al_2O_3 + AlN) [91], $CaCO_3$ [66], Al-SiC [59,137–139], Al-Ti_3AlC_2 [61], Al-TiO_2 [62], Al-B_4C-TiB_2 [70], Al-NbC [76], Al-V [63], Al-graphene/carbon SWCNTs/MWCNTs [67,68,134,135], and Al-TiB_2 [69]. The following compositions are used to synthesize copper alloy matrix composites by FSP: Cu-SiC [71], Cu-B_4C [71], Cu-TiC [71], Cu-Al_2O_3 [71], Cu-TiO_2 [72], and Cu-AlN-BN [73]. Titanium alloy matrix composites are fabricated by FSP using SiC [140] and Al_2O_3 [141]. The most frequently synthesized magnesium metal matrix composites are AZ31B-MWCNT-graphene [74], Mg-NiTi [77] and Mg-SiC-Al_2O_3 [75]. An analysis of the experimental data on FSP of structural alloys with the addition of various reinforcing particles is presented in Table 5.

Table 5. Experimental data on FSP of particle-reinforced structural alloys.

Material	FSP Parameters	Particle Introduction Method	Reinforcing Particles (size)	Average grain Size of the Base Alloy/Average Grain Size after FSP, μm	Mechanical Properties	Ref. No.
			Aluminum alloys			
Al6061	1150 rpm, 31.5 mm/min 1 pass	V-shaped grooves	SiO_2 (d_{av} = 20 nm)	-/15,53	CR: ↑ 78% ↑ MH, UTS, Elong.	[58]
Al5052	1120 rpm, 80 mm/min 1 pass	Groove (depth 2 mm, width 1 mm)	SiC (d_{av} = 5 μm)	243/5.4	MH: ↑ 29.3%	[59]
	1120 rpm, 80 mm/min 4 passes		SiC (d_{av} = 5 μm)	243/4.2	MH: ↑ 42.6%	
	1120 rpm, 80 mm/min 4 passes		SiC (d_{av} = 50 nm)	243/0.9	MH: ↑ 54.6%	
Al6061-T651	1000 rpm 72 mm/min 1 pass	Slot in the butt end of the plate	SiC (d_{av} = 3–6 μm)	-/-	UTS: ↓ 28.8% Elong.: ↓ 8.3%	[60]
	1000 rpm 72 mm/min 2 passes			-/-	UTS: ↓ 23% Elong.: ↑ 59.3%	
A356	1000 rpm 112 mm/min 1 pass	Groove	2.5 vol. % Ti_3AlC_2	-/-	MH: ↑ 18.4% UTS: ↑ 9% Elong.: ↑ 1.4 times	[61]
			5 vol. % Ti_3AlC_2	-/-	MH: ↑ 27.6% UTS: ↑ 14.2% Elong.: ↑ 1.5 times	
			7 vol. % Ti_3AlC_2	-/-	MH: ↑ 33.8% UTS: ↑ 19.4% Elong.: ↑ 1.7 times	

Table 5. *Cont.*

Material	FSP Parameters	Particle Introduction Method	Reinforcing Particles (size)	Average grain Size of the Base Alloy/Average Grain Size after FSP, μm	Mechanical Properties	Ref. No.
AA1050	1600 rpm 20 mm/min 1 pass	Holes (diameter 2.5 mm, spacing 3 mm)	TiO_2	42.85/5	MH: ↑ 61.9% CF: ↓ 19.2%	[62]
	1600 rpm 20 mm/min 2 passes		TiO_2	42.85/5	MH: ↑ 80.9% CF: ↓ 29.2%	
AA6063	1600 rpm 60 mm/min 1 pass	Grooves ($1.2 \times 5.5 \times 100$ mm^3)	12 vol. % V (d_{av} = 18 μm)	72/7.6	UTS: ↑ 24.6% Elong.: ↑ 1.2 times	[63]
AA1050	1180 rpm 80 mm/min 1 pass	Groove (width 1 mm, depth 3 mm)	Al_2O_3	128/29	-	[64]
	1180 rpm 80 mm/min 2 passes			128/23	WT: ↑ 1.8 times	
Al2024	800 rpm 25 mm/min 1 pass	Groove	Al–10 vol. % Al_2O_3 powders (d_{av} = 50–150 μm)	250 × 8/4	MH: ↑ 2.5 times WT: ↑ 3 times	[65]
AA6082	1250 rpm 40 mm/min 1 pass	-	-	141/15–20	MH: ↑ 43.5% WT: ↑ 1.2 times	[66]
		Groove (width 2 mm, depth 2 mm)	$CaCO_3$ (d_{av} = 3–5 μm)	141/10–12	MH: ↑ 35.9% WT: ↑ 1.6 times	
AA7075	1200 rpm 1 pass	Groove	5 vol. % NbC (d_{av} = 10–20 μm)	50/40	UTS: ↑ 13.6% Elong.: ↓ 20% MH: ↑ 17.3%	[76]
			10 vol. % NbC (d_{av} = 10–20 μm)	50/26	UTS: ↑ 36.3% Elong.: ↓ 30% MH: ↑ 37.7%	
			15 vol. % NbC (d_{av} = 10–20 μm)	50/16	UTS: ↑ 47.7% Elong.: ↓ 65% MH: ↑ 53%	

Table 5. *Cont.*

Material	FSP Parameters	Particle Introduction Method	Reinforcing Particles (size)	Average grain Size of the Base Alloy/Average Grain Size after FSP, μm	Mechanical Properties	Ref. No.
AA7075	800 rpm 60 mm/min 1 pass	Hole (diameter 2 mm, depth 3 mm)	-	82.70/2.98	MH: ↓ 11.8% IT: ↓ 37.9%	[67]
			MWCNT (diameter 15–20 nm, length 5 μm)	82.70/2.88	MH: ↑ 2.8% IT: ↓ 29.7%	
			Cu (d_{av} = 10–20 μm)	82.70/2.57	MH: ↑ 6.9% IT: ↓ 8.8%	
			SiC (d_{av} = 15–20 μm)	82.70/2.53	MH: ↑ 2.8% IT: ↓ 6.3%	
AA1060	950 rpm 30 mm/min 3 passes	-	-	-/4.8	UTS: 90.2 MPa Elong.: 36.8%	[68]
	950 rpm 150 mm/min 3 passes	3 plates, groove in the middle plate (length 150 mm, depth 1.5 mm)	1.6 vol. % CNT (diameter 12.1 nm, length 1 μm)	-/-	UTS: 102.3 MPa Elong.: 25.3%	
	600 rpm 95 mm/min 3 passes			-/-	UTS: 103.4 MPa Elong.: 33.4%	
	750 rpm 30 mm/min 3 passes			-/-	UTS: 110.9 MPa Elong.: 32.3%	
	600 rpm 150 mm/min 3 passes	3 plates, groove in the middle plate (length 150 mm, depth 2 mm)	3.2 vol. % CNT (diameter 12.1 nm, length 1 μm)	-/1.9	UTS: 93.6 MPa Elong.: 32.1%	
	750 rpm 95 mm/min 3 passes			-/2.1	UTS: 127 MPa Elong.: 23.3%	
	950 rpm 30 mm/min 3 passes			-/3.3	UTS: 138.8 MPa Elong.: 31.2%	

Table 5. *Cont.*

Material	FSP Parameters	Particle Introduction Method	Reinforcing Particles (size)	Average grain Size of the Base Alloy/Average Grain Size after FSP, μm	Mechanical Properties	Ref. No.
AA6061	1000 rpm 340 mm/min 1 pass	-	-	70/20	MH: ↑ 15.4% UTS: ↑ 10% Elong.: ↑ 20.8% CF: ↓ 8.7%	[69]
	1000 rpm 340 mm/min 4 passes	Groove 2×3 mm^2	Micro-sized TiB_2 particles and nano-sized graphene platelets: 10 wt. % TiB_2–0 wt. % graphene	70/< 1 μm	MH: ↑ 31.6% UTS: ↑ 18.1% Elong.: ↓ 16.6% CF: ↓ 14%	
			20 wt. % TiB_2–0 wt. % graphene		MH: ↑ 48.2% UTS: ↑ 31.3% Elong.: ↓ 25% CF: ↓ 26.3%	
			30 wt. % TiB_2–0 wt. % graphene		MH: ↑ 45% UTS: ↑ 45% Elong.: ↓ 50% CF: ↓ 7%	
			0 wt. % TiB_2–0.5 wt. % graphene		MH: ↑ 22.1% UTS: ↑ 37.5% Elong.: ↑ 4.2% CF: ↓ 12%	
			0 wt. % TiB_2–1 wt. % graphene		MH: ↑ 37.5% UTS: ↑ 54.4% Elong.: ↑ 20.8% CF: ↓ 24.5%	
			0 wt. % TiB_2–2 wt. % graphene		MH: ↑ 38.5% UTS: ↑ 59.4% Elong.: ↓ 16.7% CF: ↓ 3.5%	
			20 wt. % TiB_2–0.5 wt. % graphene		MH: ↑ 54.4% UTS: ↑ 61.9% Elong.: ↓ 8.3% CF: ↓ 29.8%	
			20 wt. % TiB_2–1 wt. % graphene		MH: ↑ 66.5% UTS: ↑ 69.4% Elong.: ↓ 4.2% CF: ↓ 29.6%	
			20 wt. % TiB_2–2 wt. % graphene		MH: ↑ 62.8% UTS: ↑ 75.6% Elong.: ↓ 62.5% CF: ↓ 1.7%	

Table 5. *Cont.*

Material	FSP Parameters	Particle Introduction Method	Reinforcing Particles (size)	Average grain Size of the Base Alloy/Average Grain Size after FSP, μm	Mechanical Properties	Ref. No.
Al7005	750 rpm 50 mm/min 2 passes	-	-	-/-	MH: ↑ 33.3%	[70]
		Holes (diameter 1.5 mm, depth 3 mm)	50% B_4C + 50% TiB_2 75% B_4C + 25% TiB_2 25% B_4C + 75% TiB_2	-/- -/- -/-	MH: ↑ 66.6% MH: ↑ 64.4% MH: ↑ 61.1%	
Copper alloys						
Cu (99.9%)	1000 rpm 40 mm/min 1 pass	Groove (depth 2.5 mm, width 0.7 mm)	12 vol. % SiC 12 vol. % Al_2O_3 12 vol. % B_4C 12 vol. % TiC	35/6 35/3 35/5 35/4	MH: ↑ 54.6% MH: ↑ 58.6% MH: ↑ 80% MH: ↑ 68%	[71]
Cu (99.9%)	710 rpm 20 mm/min 1 pass	-	-	30/21	MH: ↑ 8% UTS: ↑ 2.5% Elong.: ↓ 1.9 time CF: ↓ 14%	[72]
	710 rpm 20 mm/min 1 pass	Holes (depth 3 mm, length 2 mm, spacing 4 mm)	TiO_2 (d_{av} = 41 nm)	30/9.3	MH: ↑ 28.3% UTS: ↑ 22.6% Elong.: ↓ 2.7 time CF: ↓ 48.4%	
	710 rpm 20 mm/min 2 passes			30/6.4	MH: ↑ 50% UTS: ↑ 27.6% Elong.: ↓ 3.5 time CF: ↓ 60.9%	
	710 rpm 20 mm/min 4 passes			30/2.4	MH: ↑ 77% UTS: ↑ 33% Elong.: ↓ 2.4 time CF: ↓ 75%	
Cu	1000 rpm 30 mm/min 1 pass	Groove	AlN (d_{av} = 10 μm), BN (d_{av} = 1 μm): 5 vol. % (25 mass. % AlN + 75 mass. % BN)	-/-	MH: ↑ 25% UTS: ↓ 26.6% Elong.: ↓ 1.4 times	[73]
			AlN (d_{av} = 10 μm), BN (d_{av} = 1 μm): 10 vol. % (25 mass. % AlN + 75 mass. % BN)	-/-	MH: ↑ 28.3% UTS: ↓ 19.7% Elong.: ↓ 1.5 times	
			AlN (d_{av} = 10 μm), BN (d_{av} = 1 μm): 15 vol. % (25 mass. % AlN + 75 mass. % BN)	-/-	MH: ↑ 29.2% UTS: ↓ 19.7% Elong.: ↓ 2.3 time	

Table 5. *Cont.*

Material	FSP Parameters	Particle Introduction Method	Reinforcing Particles (size)	Average grain Size of the Base Alloy/Average Grain Size after FSP, μm	Mechanical Properties	Ref. No.
			Titanium alloys			
CP-Ti	800 rpm 45 mm/min 3 passes	-	-	75/4	MH: ↑ 56.2%	[140]
	500 rpm 50 mm/min 4 passes	Grooves (width 2 mm, depth 2 mm)	β-SiC powder (d_{av} = 50 nm)	75/0.4	MH: ↑ 228%	
CP-Ti grade 2	500 rpm 50 mm/min 1 pass	-	-	28/4.4	-	[141]
	500 rpm 50 mm/min 4 passes	-	-	28/2.6	-	
	500 rpm 50 mm/min 1 pass	Groove (width 1 mm, depth 3 mm)	~1.8 vol. % Al_2O_3 (d_{av} = 80 nm)	28/1.14	-	
			Magnesium alloys			
AZ31B	1000 rpm 40 mm/min 3 passes	Groove 2 × 4 mm^2	1.6 vol. % MWCNT (d_{av} = 10–30 nm) + 0.3 vol. % graphene (d_{av} = 5–10 nm)	-/-		[74]
	1200 rpm 40 mm/min 3 passes			-/-		
	1400 rpm 40 mm/min 3 passes			-/-		

Table 5. *Cont.*

Material	FSP Parameters	Particle Introduction Method	Reinforcing Particles (size)	Average grain Size of the Base Alloy/Average Grain Size after FSP, μm	Mechanical Properties	Ref. No.
Mg + 5 wt. % ($SiC + Al_2O_3$)	SiC and Al_2O_3 hybrid particles were added to molten metal at 700 °C. The mixture was stirred for 20 min at 400 rpm with a stirrer, followed by pouring into a permanent mould	Casting	5 wt. % ($SiC + Al_2O_3$)	82	MH: 59.3 HV	[75]
	220 rpm 10 mm/min 1 pass			82/15	MH: ↑ 13.9%	
	340 rpm 20 mm/min 1 pass			82/11	MH: ↑ 15.5%	
	560 rpm 30 mm/min 1 pass			82/7	MH: ↑ 17.5%	

FSP of structural alloys allows the formation of gradient composite structures with the hardness increased by 13–80%, tensile strength by 2.5–75%, compressive strength by 70%, and wear resistance by 14–26% compared to the base metal (Table 5). As can be seen from Table 5, the tensile ductility values of many particle-reinforced structural alloys are lower than those of the base metals. The tensile characteristics depend on many microstructural factors such as the interaction between the base metal matrix and reinforcing particles, the particle size distribution in the processed area, and the dislocation density. The main reason for the deteriorated tensile strength of simply processed and reinforced materials as compared to the base metals is the residual stresses induced by the enormous heat release in FSP [74]. In addition, the presence of hard reinforcing particles inside the grains and at the grain boundaries causes high stress concentrations in zones with harder particles prone to crack initiation and growth, as a result of which the material ductility is reduced [74]. An analysis of Table 5 also shows increased hardness for all FSPed particle-reinforced structural alloys, despite some cases when both ductility and tensile strength are reduced. In most experimental studies, the hardness enhancement is attributed to grain refinement and the presence of fine reinforcing particles in accordance to the Hall-Petch and Orowan mechanisms, respectively [68,72,138,142]. In addition, as a result of increasing dispersion of reinforcement particles the distance between them is reduced and therefore the free run length of dislocations is restricted. The restriction of dislocation motion also contributes to higher microhardness of surface composites.

5. Friction Stir Processing of Structural Alloys for Fabricating In Situ Hybrid Surfaces

Of greatest interest in the last decade is the fabrication of hybrid composites by in situ reactions during FSP. The given FSP technique provides almost complete mixing of the introduced powder with the plasticized substrate metal due to a complex quasi-viscous material flow at temperatures below the melting point. The in situ hybrid composite FSP method has several advantages over other FSP methods used for composite fabrication: (1) more thermodynamically stable matrix reinforcement [143], (2) coherent/semi-coherent bonding at the particle/matrix interfaces (Figure 10) [60,79,136], and (3) formation of finer reinforcing particles uniformly distributed in the matrix [82]. The interfacial characteristics, including the interfacial bonding structure, intermediate phase formation, and thermal expansion difference, are also fundamental and depend on the chemical composition of both the introduced particles and the matrix. The complexity of interfacial reactions affects the adhesion between particles and the matrix, which has an additional effect on the mechanical properties of in situ hybrid composites. The high strain rate and friction during FSP produce a large amount of heat, the material temperature rises, resulting in a higher diffusion rate and shorter diffusion distances. All these factors accelerate the in situ exothermic reactions between the metal matrix atoms and the introduced particles. Since the reactions are exothermic, there is additional heat release that also contributes to the temperature rise and reaction acceleration. High strains and temperatures reached during FSP cause fragmentation and dissolution of the reinforcing particles, which leads to further precipitation of smaller intermetallic particles and their more uniform distribution in the matrix.

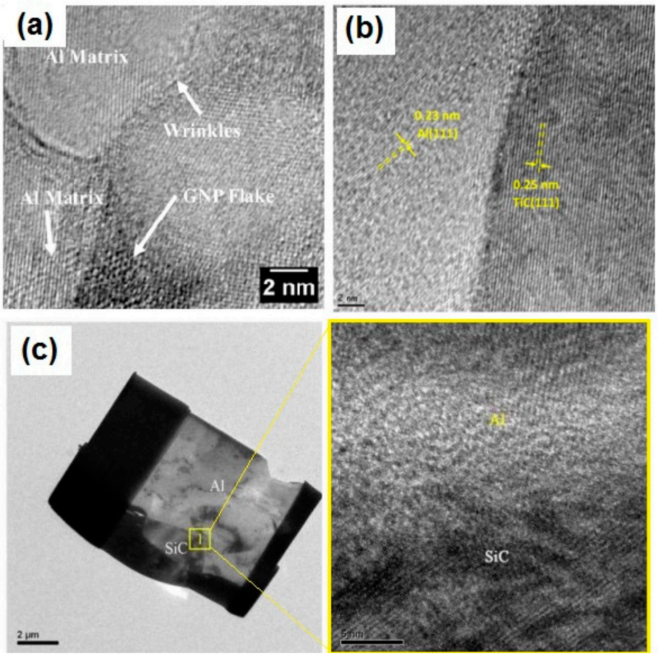

Figure 10. Coherent and semi-coherent interfaces between the matrix and reinforcing particles: (**a**) TEM-BF images of FSPed A356 reinforced with graphene nanoplatelets (GNP) showing the interface between the matrix and encapsulated GNP flakes (reproduced from [136], with permission from Elsevier, 2020); (**b**) HRTEM micrograph of the particle/matrix interface in the six-pass FSPed composite (reproduced from [79], with permission from Elsevier,2019); (**c**) HRTEM micrographs of the stir zone containing bare SiC reinforcement (reproduced from [60], with permission from authors, 2018).

As noted by Zhang et al. [143], the heat release of the metal/metal oxide reaction is much higher than that of the metal/transition metal reaction. Therefore, a reaction with enhanced formation kinetics is expected for the metal/metal oxide system. Moreover, the formation of nano-sized reaction products with coherent or semi-coherent interfaces can improve the mechanical properties. Experimental studies showed that in situ hybrid composites can be fabricated by FSP using the systems Al-CeO_2 [96], Al-TiO_2 [143], Al + Mg + CuO [98], and Al-$Al_{13}Fe_4$-Al_2O_3 [82]. In many oxide/aluminum substitution reactions, the reduced metal can exothermically react with Al to form an intermetallic compound, due to which the system temperature rises [82]. As was shown for an aluminum-based in situ composite synthesized from an Al-Mg-CuO powder mixture by FSP, the use of the Mg/metal oxide substitution reaction instead of the Al/metal oxide one has a positive effect on the synthesized aluminum-based in situ nanocomposites [98]. The nano-sized MgO and Al_2Cu particle-reinforced composite exhibits an excellent Young's modulus (88 GPa) and yield strength (350 MPa in tension and 436 MPa in compression) [98].

In the work by Azimi-Roeen et al. [82], pre-milled powder mixture ($Al_{13}Fe_4$ + Al_2O_3) was introduced into the stir zone formed in a 1050 aluminum alloy sheet by FSP. The homogeneous and active mixture reacted with plasticized aluminum to form $Al_{13}Fe_4$ + Al_2O_3 particles. The intermetallic $Al_{13}Fe_4$ was represented by elliptical particles of ~100 nm in size, and nano-sized Al_2O_3 precipitated in the form of flocculated particles with the remnants of iron oxide particles. With increasing milling time (1–3 h) of the introduced powder mixture, the volume fraction of $Al_{13}Fe_4$ + Al_2O_3 increased in the fabricated composite. The hardness and tensile strength of the nanocomposites varied from 54.5 HV to 75 HV and from 139 MPa to 159 MPa, respectively (Table 6) [82].

Table 6. Experimental data on FSP of in situ hybrid composites.

Material	FSP Parameters	Particle Introduction Method	Introduced Particles (Size)	Average Grain Size of the Base Alloy/Average Grain Size after FSP, μm	Formation of Additional/Intermetallic Phases	Mechanical Properties	Ref. No.
Aluminum alloys							
7075	1200 rpm 30 mm/min 1 pass	Groove (width 3 mm, depth 3 mm)	Ti-6Al-4V (d_{av} = 35 nm)	-/-	Al_3Ti AlTi $AlTi_3$	MH: ↑ 3.3% UTS: ↑ 7.4% Elong.: ↑ 1.2 times FC: 0.7	[78]
	1200 rpm 30 mm/min 2 passes		Ti-6Al-4V (d_{av} = 35 nm)	-/-	Al_3Ti AlTi $AlTi_3$	MH: ↑ 28.3% UTS: ↑ 23.5% Elong.: ↑ 2 times FC: 0.58	
	1200 rpm 30 mm/min 3 passes		Ti-6Al-4V (d_{av} = 35 nm)	-/-	Al_3Ti AlTi $AlTi_3$	MH: ↑ 60% UTS: ↑ 38.8% Elong.: ↑ 2.1 times FC: 0.32	
AA1050	1400 rpm 40 mm/min 2 passes	Holes (diameter 2 mm, depth 3 mm	Ni (≤ 20 μm), Ti (40-60 μm), C (50 μm). Powder mixture Ni-32 mass. % Ti-8 mass. % C. Preliminary planetary ball milling	-/-	Al_3Ni TiC	-	[79]
	1400 rpm 40 mm/min 4 passes			-/-	Al_3Ni TiC	-	
	1400 rpm 40 mm/min 6 passes			-/-	Al_3Ni TiC	MH: ↑ 214%	
Al6061-T651	1000 rpm 72 mm/min 1 pass	Slot in the butt end of the plate	SiC (d_{av} = 3-6 μm) with 1.3–1.8 μm thick copper coating	-/-	Al_2Cu Al_4Cu_9	MH: ↓ 11% UTS: ↓ 24.6% Elong.: ↑ 18.7%	[60]
	1000 rpm 72 mm/min 2 passes		SiC (d_{av} = 3–6 μm) with 1.3–1.8 μm thick copper coating	-/-	Al_2Cu Al_4Cu_9	MH: ↑ 16.6% UTS: ↓ 15% Elong.: ↑ 29.6%	

Table 6. *Cont.*

Material	FSP Parameters	Particle Introduction Method	Introduced Particles (Size)	Average Grain Size of the Base Alloy/Average Grain Size after FSP, μm	Formation of Additional/Intermetallic Phases	Mechanical Properties	Ref. No.
A356	1600 rpm 50 mm/min 1 pass	Groove (width 0.6 mm, depth 3.5 mm)	Powder mixture SiCp (d_{av} = 30 μm) – MoS_2 (d_{av} = 5 μm)	Destruction of needle-like Si and Al dendrites	SiCp and MoS_2 particles (d_{av} ~10 μm)	MH: ↑ 45.4% FC: ↓ 2 times	[80]
	1600 rpm 50 mm/min 1 pass	Groove (width 0.6 mm, depth 3.5 mm)	SiCp (d_{av} = 30 μm)	Destruction of needle-like Si and Al dendrites	SiCp particles (d_{av} ~10 μm)	MH: ↑ 54.5%	
A6061	1600 rpm 60 mm/min 2 passes	Groove dimensions correspond to 18 vol.% of reinforcing particles	18 vol. % fly ash (d_{av} = 5 μm)	76.85/5.61	Uniform distribution of fly ash particles independently of the metal matrix type	MH: ↑ 2 times	[81]
1050	1120 rpm 125 mm/min 4 passes	Groove (depth 3.5 mm, width 1.4 mm)	Powder mixture Fe_2O_3 (d_{av} = 1 μm) – Al (d_{av} = 100 μm), pre-mixed and pre-ground	-/~2–3	$Al_{13}Fe_4$ (~100 nm) α-Al_2O_3, Fe_3O_4	MH: ↑ 27.3%	[82]
Al-1050-H24	750 rpm 99.4 mm/min	Groove (width 3 mm, depth 1.5 mm)	Cu powder (d_{av} = 5 μm)	-/-	$CuAl_2$ Al-Cu Al_4Cu_9	MH: ↑ 4 times	[83]
	750 rpm 49.7 mm/min			-/-		MH: ↑ 5 times	
A413	2000 rpm 8 mm/min 1 pass	Groove 2 × 3 mm^2	Ni powder (d_{av} = 1–3 μm)	Si: 40.6/4.58	Al_3Ni	MH: ↑ 18.8% CF: ↓ 1.5 times	[84]
	2000 rpm 8 mm/min 3 passes			Si: 40.6/2.8		MH: ↑ 26.5% CF: ↓ 1.5 times	

Table 6. *Cont.*

Material	FSP Parameters	Particle Introduction Method	Introduced Particles (Size)	Average Grain Size of the Base Alloy/Average Grain Size after FSP, μm	Formation of Additional/Intermetallic Phases	Mechanical Properties	Ref. No.
Al1100	1180 rpm 60 mm/min 2 passes	Groove (width 3 mm, depth 5 mm)	Ni powder (d_{av} = 25–38 μm)	-/-	Nonuniform distribution of a small amount of Al_3Ni particles	MH: ↑ 1.8 times UTS: ↑ 1.5 times Elong.: ↓ 1.9 times	[85]
	1180 rpm 60 mm/min 4 passes			-/-	More uniform distribution of Al_3Ni	MH: ↑ 2.5 times UTS: ↑ 1.8 times Elong.: ↓ 3.5 times	
	1180 rpm 60 mm/min 6 passes			-/-	Uniform Al_3Ni distribution (d_{av} ≤ 1 μm)	MH: ↑ 2.7 times UTS: ↑ 1.9 times Elong.: ↓ 3.9 times	
Al1050	1600 rpm 20 mm/min 2 passes	Groove 1 × 2 × 160 mm^3	Nb powder (d = 1–10 μm)	60/23	Al_3Nb	MH: ↑ 13.6% UTS: ↑ 13.3% Elong.: ↓ 2.5 times	[86]
	1600 rpm 20 mm/min 4 passes	Groove 1 × 2 × 160 mm^3		60/6.5	Al_3Nb	MH: ↑ 54.5% UTS: ↑ 33.3% Elong.: ↓ 1.6 times	
	1600 rpm 20 mm/min 4 passes	Groove 2 × 2 × 160 mm^3		60/4	Al_3Nb	MH: ↑ 100% UTS: ↑ 33.3% Elong.: ↓ 2 times	
AA5052	1250 rpm 25 mm/min 1 pass	-	-	10.7/9.7	-	MH: ↑ 9% UTS: ↑ 14.4% Elong.: ↓ 3.4%	[87]
	1200 rpm 100 mm/min 5 passes	Groove (width 1.2 mm, depth 3.5 mm)	Powders of graphene nanoplatelets (diameter 2 μm, thickness 1–20 nm)	10.7/2.1	$(Fe,Mn,Cr)_3SiAl_{12}$ particles (d_{av} ≤ 1 μm), Al_4C_3 particles	MH: ↑ 52.7% UTS: ↑ 35.7% Elong.: ↓ 31.8%	

Table 6. *Cont.*

Material	FSP Parameters	Particle Introduction Method	Introduced Particles (Size)	Average Grain Size of the Base Alloy/Average Grain Size after FSP, μm	Formation of Additional/Intermetallic Phases	Mechanical Properties	Ref. No.
Copper alloys							
Cu plate (99.9% pure)	1000 rpm 40 mm/min 2 passes	Groove dimensions correspond to 18 vol. % of reinforcing particles	18 vol. % fly ash (d_{av} = 5 μm)	35.43/2.79	Uniform distribution of fly ash particles independently of the metal matrix type	MH: ↑ 2.13 times	[81]
Titanium alloys							
Ti-6Al-4V	800 rpm 25 mm/min 1 pass	-	-	-/-	-	MH: ↑ 5.4% CS: ↑ 1.7%	[88]
		Holes (diameter 1.2 mm, depth 3.8 mm, spacing 2.5 mm)	B_4C (d_{av} = 10 μm)	-/-	TiB, TiB_2, TiC	MH: ↑ 68% CS: ↑ 47.9%	
Ti	1200 rpm 50 mm/min 1 pass	-	-	92.2/~2	-	MH: ↑ 25.5% UTS: ↑ 28.8% Elong.: ↓ 33.7%	[89]
		Groove (length 210 mm, width 1.2 mm, depth 3.5 mm)	Hydroxy-apatite powder $Ca_{10}(PO_4)_6(OH)_2$ (d_{av} = 120 nm)	92.2/1.4–14.8	Decomposition products in the form of elemental calcium (Ca) and phosphide (PO_3)	MH: ↑ 34.8% UTS: ↓ 41.6% Elong.: ↓ 52.2%	
Magnesium alloys							
AZ31	1200 rpm 40 mm/min 2 passes	Groove dimensions correspond to 18 vol.% of reinforcing particles	18 vol.% fly ash (d_{av} = 5 μm)	66.35/6.09	Uniform distribution of fly ash particles independently of the metal matrix type	MH: ↑ 1.75 times	[81]

In the case of an incoherent bonding interface between particles and the metal matrix, the surface characteristics of the particles can be modified by additional processing, e.g., by plating. Huang and Aoh [60] performed electroless plating to deposit a copper coating on the surface of SiC ceramic particles to change their surface characteristics. The preliminary processing of the particles provided interphase coherence through the formation of Al_2Cu and Al_4Cu_9 intermetallic compounds at the interphase boundary. Double-pass FSP with the Cu-coated reinforcement increased the composite hardness and ductility by about 20% (Figure 11, Table 6).

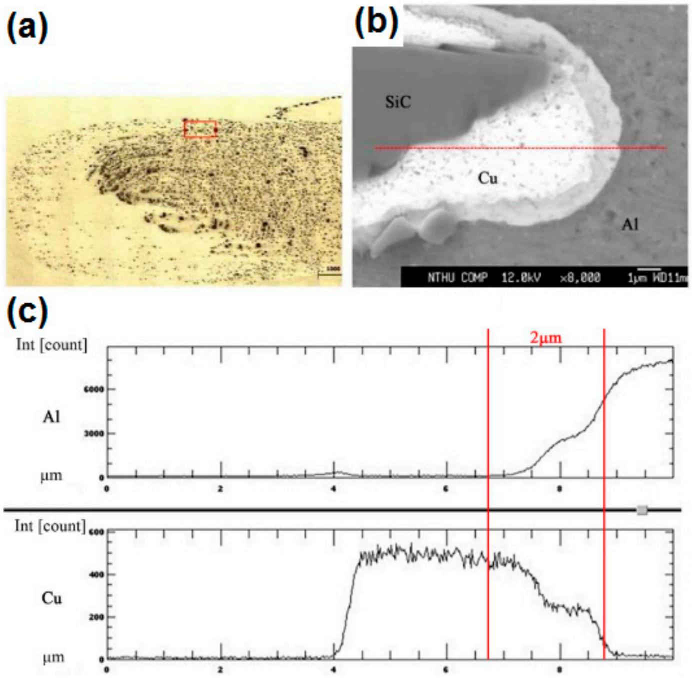

Figure 11. Micrographs of copper-coated SiC particles embedded in the matrix (**a**,**b**); Al-SiC/Cu reinforcement with EPMA line scan across Cu-coated SiC and Al matrix showing Al and Cu distribution (**c**) (reproduced from [60], with permission from authors, 2018).

The FSP method is also used to fabricate in situ metal matrix composites of the compositions Al-Al_2Cu [60], Al-Al_3Ti [78], Al-$Al_{13}Fe_4$ [82], Al-Al_3Ni [79,84,85] with the formation of intermetallic phases. Such composites are mainly synthesized using powder mixtures subjected to pre-processing and special preparation. For an FSPed A413 alloy reinforced by Ni powder, Golmohammadi et al. [88] observed the destruction of needle-like Si particles and in situ formation of uniformly distributed intermetallic Al_3Ni particles. An increase in the number of FSP passes led to less agglomeration, finer and more uniform dispersion of reinforcing particles, as well as to an increase in the intermetallic phase length. The authors showed that the wear resistance of the Al-Al3Ni composite is higher by approximately a factor of 2 than that of the base alloy (Table 6) [84].

Experiments showed that the addition of carbon-based solid lubricating particles (graphene particles and platelets, nanotubes, fibers, etc.) together with hard particles improves the tribological behavior of in situ composites under sliding wear conditions [69,80,87]. Dixit et al. [144] synthesized new multi-layer graphene-reinforced aluminum composites by exfoliating cheap graphite into graphene using friction stir alloying, and observed a twofold increase in strength. This method opened up new possibilities for the efficient and scalable production of graphene-based metal matrix nanocomposites [144].

Experimental studies were performed for FSPed in situ composites on the basis of aluminum alloys: Al7075-Ti-6Al-4V [78], Al1050-Ni-Ti-C [79], Al-SiC [60,80], Al6061-fly ash [81,90], Al1050-Fe_2O_3-Al [82], Al-1050-Cu [83], Al-Ni [84,85], Al-Nb [86], Al-graphene [69,80,87]; copper alloys: Cu-fly ash [81]; titanium alloys: Ti-6Al-4V-B_4C [81], Ti-hydroxyapatite powder [89]; magnesium alloys: AZ31-fly ash [81]. A review of the experimental data on FSP of in situ hybrid composite materials is given in Table 6.

6. Conclusions

This paper summarizes the latest progress in the study of friction stir processing of aluminum, copper, titanium, and magnesium alloys. Severe plastic deformation and thermal effects during FSP cause the destruction of large dendrites and second phase particles, grain refinement in the matrix, elimination of porosity, as well as the formation of a homogeneous fine-grained structure. It was shown that FSP can be applied to fabricate metallic materials:

(1) with a subsurface gradient structure obtained through the formation of equiaxed nanograins and structural homogenization;
(2) with a compositional subsurface gradient structure formed by modifying and hardening the material surface with reinforcing particles;
(3) in situ composites.

FSP of structural alloys proves to be the most energy efficient, environmentally friendly, and versatile method that allows local controlled modification of the subsurface microstructure in the processed structural materials.

However, the literature contains a wide scatter of experimental results on the properties of FSPed metallic materials, indicating the necessity of further research in this relevant area. A reason for the large data scatter can be the physical nature of the friction stir process based on the phenomenon of adhesion friction, which is of highly inhomogeneous nature as compared to lubricated friction. In view of the frictional inhomogeneity, it is possible to fabricate materials with markedly different properties by using slightly different FSP tool geometries at the same processing parameters. Despite the presence of unresolved issues concerning the FSP of structural alloys, the given method shows much promise for commercial applications.

Author Contributions: Resources, writing part 1–3, 6, A.P.Z.; writing part 4, A.V.C.; writing part 5, S.Y.T.; guidance and corrections to the article, E.A.K. All authors have read and agreed to the published version of the manuscript.

Funding: A review of references of friction stir processing of alloys, hardening with various reinforcing particles, fabrication of hybrid and in situ surfaces was funded by Government research assignment for ISPMS SB RAS, project No. III.23.2.11. A review of references of friction stir processing of aluminum and copper alloys was performed with financial support from RSF Grant No. 19-79-00136.

Conflicts of Interest: The authors declare no conflict of interest.

Nomenclature

FSP	friction stir processing
FSW	friction stir welding
MH	microhardness
UTS	ultimate tensile strength
Elong	elongation
WT	wear testing
CR	corrosion resistance
IT	impact toughness
SWCNTs	single-walled carbon nanotubes
MWCNT	multi-walled carbon nanotubes
CNTs	carbon nanotubes
CS	compressive strength
HRTEM	high resolution transmission electron microscopy

References

1. Hekimoğlu, A.P.; Çalış, M.; Ayata, G. Effect of Strontium and Magnesium Additions on the Microstructure and Mechanical Properties of Al–12Si Alloys. *Met. Mater. Int.* **2019**, *25*, 1488–1499. [CrossRef]
2. He, T.; Chen, W.; Wang, W.; Ren, F.; Stock, H.R. Effect of different Cu contents on the microstructure and hydrogen production of Al–Cu-Ga-In-Sn alloys for dissolvable materials. *J. Alloys Compd.* **2020**, *821*, 153489. [CrossRef]
3. Trudonoshyn, O.; Rehm, S.; Randelzhofer, P. Körner Improvement of the high-pressure die casting alloy Al-5.7Mg-2.6Si-0.7Mn with Zn addition. *Mater. Charact.* **2019**, *158*, 109959. [CrossRef]
4. Prach, O.; Trudonoshyn, O.; Randelzhofer, P.; Körner, C.; Durst, K. Effect of Zr, Cr and Sc on the Al–Mg–Si–Mn high-pressure die casting alloys. *Mater. Sci. Eng. A* **2019**, *759*, 603–612. [CrossRef]
5. Fabrizi, A.; Ferraro, S.; Timelli, G. The influence of Sr, Mg and Cu addition on the microstructural properties of a secondary AlSi9Cu3(Fe) die casting alloy. *Mater. Charact.* **2013**, *85*, 13–25. [CrossRef]
6. Seifeddine, S.; Johansson, S.; Svensson, I.L. The influence of cooling rate and manganese content on the β-Al_5FeSi phase formation and mechanical properties of Al–Si-based alloys. *Mater. Sci. Eng. A* **2008**, *490*, 385–390. [CrossRef]
7. Rao, Y.; Yan, H.; Hu, Z. Modification of eutectic silicon and β-Al5FeSi phases in as-cast ADC12 alloys by using samarium addition. *J. Rare Earths* **2013**, *31*, 916–922. [CrossRef]
8. Cinkilic, E.; Ridgeway, C.D.; Yan, X.; Luo, A.A. A Formation Map of Iron-Containing Intermetallic Phases in Recycled Cast Aluminum Alloys. *Metall. Mater. Trans. A Phys. Metall. Mater. Sci.* **2019**, *50*, 5945–5956. [CrossRef]
9. Irizalp, S.G.; Saklakoglu, N. Effect of Fe-rich intermetallics on the microstructure and mechanical properties of thixoformed A380 aluminum alloy. *Eng. Sci. Technol. Int. J.* **2014**, *17*, 58–62. [CrossRef]
10. Mohamed, A.M.A.; Samuel, A.M.; Samuel, F.H.; Doty, H.W. Influence of additives on the microstructure and tensile properties of near-eutectic Al–10.8%Si cast alloy. *Mater. Des.* **2009**, *30*, 3943–3957. [CrossRef]
11. Li, Q.; Xia, T.; Lan, Y.; Zhao, W.; Fan, L.; Li, P. Effect of in situ γ-Al2O3 particles on the microstructure of hypereutectic Al–20%Si alloy. *J. Alloys Compd.* **2013**, *577*, 232–236. [CrossRef]
12. Huang, X.; Yan, H. Effect of trace la addition on the microstructure and mechanical property of as-cast ADC12 Al-Alloy. *J. Wuhan Univ. Technol. Mater. Sci. Ed.* **2013**, *28*, 202–205. [CrossRef]
13. Li, J.H.; Wang, X.D.; Ludwig, T.H.; Tsunekawa, Y.; Arnberg, L.; Jiang, J.Z.; Schumacher, P. Modification of eutectic Si in Al–Si alloys with Eu addition. *Acta Mater.* **2015**, *84*, 153–163. [CrossRef]
14. Czerwinski, F. Cerium in aluminum alloys. *J. Mater. Sci.* **2020**, *55*, 24–72. [CrossRef]
15. Niu, G.; Mao, J.; Wang, J. Effect of Ce Addition on Fluidity of Casting Aluminum Alloy A356. *Metall. Mater. Trans. A Phys. Metall. Mater. Sci.* **2019**, *50*, 5935–5944. [CrossRef]
16. Ravi, M.; Pillai, U.T.S.; Pai, B.C.; Damodaran, A.D.; Dwarakadasa, E.S. The effect of mischmetal addition on the structure and mechanical properties of a cast Al-7Si-0.3Mg alloy containing excess iron (up to 0.6 pct). *Metall. Mater. Trans. A Phys. Metall. Mater. Sci.* **2002**, *33*, 391–400. [CrossRef]
17. Bijalwan, P.; Pandey, K.K.; Mukherjee, B.; Islam, A.; Pathak, A.; Dutta, M.; Keshri, A.K. Tailoring the bimodal zone in plasma sprayed CNT reinforced YSZ coating and its impact on mechanical and tribological properties. *Surf. Coat. Technol.* **2019**, *377*, 124870. [CrossRef]
18. Gui, M.; Kang, S.B.; Euh, K. Influence of spraying conditions on microstructures of Al-SiCpcomposites by plasma spraying. *Metall. Mater. Trans. A* **2005**, *36*, 2471–2480. [CrossRef]
19. Maharajan, S.; Ravindran, D.; Rajakarunakaran, S.; Khan, M.A. Analysis of surface properties of tungsten carbide (WC) coating over austenitic stainless steel (SS316) using plasma spray process. *Mater. Today Proc.* **2019**. [CrossRef]
20. Xi, H.; He, P.; Wang, H.; Liu, M.; Chen, S.; Xing, Z.; Ma, G.; Lv, Z. Microstructure and mechanical properties of Mo coating deposited by supersonic plasma spraying. *Int. J. Refract. Met. Hard Mater.* **2020**, *86*, 105095. [CrossRef]
21. Padmini, B.V.; Mathapati, M.; Niranjan, H.B.; Sampathkumaran, P.; Seetharamu, S.; Ramesh, M.R.; Mohan, N. High temperature tribological studies of cold sprayed nickel based alloy on low carbon steels. *Mater. Today Proc.* **2019**. [CrossRef]

22. Liu, Z.; Wang, H.; Haché, M.; Irissou, E.; Zou, Y. Formation of refined grains below 10 nm in size and nanoscale interlocking in the particle–particle interfacial regions of cold sprayed pure aluminum. *Scr. Mater.* **2020**, *177*, 96–100. [CrossRef]
23. Dabney, T.; Johnson, G.; Yeom, H.; Maier, B.; Walters, J.; Sridharan, K. Experimental evaluation of cold spray FeCrAl alloys coated zirconium-alloy for potential accident tolerant fuel cladding. *Nucl. Mater. Energy* **2019**, *21*, 100715. [CrossRef]
24. Hu, C.; Baker, T.N. A new aluminium silicon carbide formed in laser processing. *J. Mater. Sci.* **1997**, *32*, 5047–5051. [CrossRef]
25. Pantelis, D.; Tissandier, A.; Manolatos, P.; Ponthiaux, P. Formation of wear resistant Al–SiC surface composite by laser melt–particle injection process. *Mater. Sci. Technol.* **1995**, *11*, 299–303. [CrossRef]
26. Katipelli, L.R.; Dahotre, N.B. Mechanism of high temperature oxidation of laser surface engineered TiC/Al alloy 'composite' coating on 6061 aluminium alloy. *Mater. Sci. Technol.* **2001**, *17*, 1061–1068. [CrossRef]
27. Dong, M.; Cui, X.; Lu, B.; Jin, G.; Cai, Z.; Feng, X.; Liu, Z.; Wang, H. Effect of Ti+N and Zr+N ions implantation on mechanical and corrosion performance of carburized layer. *Thin Solid Films* **2019**, *692*, 137597. [CrossRef]
28. Chen, T.; Castanon, E.; Gigax, J.G.; Kim, H.; Balerio, R.; Fan, J.; Garner, F.A.; Shao, L. Nitrogen ion implantation into pure iron for formation of surface nitride layer. *Nucl. Instruments Methods Phys. Res. Sect. B Beam Interact. Mater. Atoms* **2019**, *451*, 10–13. [CrossRef]
29. Acciari, H.A.; Palma, D.P.S.; Codaro, E.N.; Zhou, Q.; Wang, J.; Ling, Y.; Zhang, J.; Zhang, Z. Surface modifications by both anodic oxidation and ion beam implantation on electropolished titanium substrates. *Appl. Surf. Sci.* **2019**, *487*, 1111–1120. [CrossRef]
30. Titov, A.I.; Karaseov, P.A.; Karabeshkin, K.V.; Ermolaeva, G.M.; Shilov, V.B. Effect of monatomic and molecular ion irradiation on time resolved photoluminescence decay in GaN. *Nucl. Instruments Methods Phys. Res. Sect. B Beam Interact. Mater. Atoms* **2019**, *458*, 164–168. [CrossRef]
31. Stepanov, A.L.; Vorobev, V.V.; Rogov, A.M.; Nuzhdin, V.I.; Valeev, V.F. Sputtering of silicon surface by silver-ion implantation. *Nucl. Instruments Methods Phys. Res. Sect. B Beam Interact. Mater. Atoms* **2019**, *457*, 1–3. [CrossRef]
32. Kalashnikov, M.P.; Fedorischeva, M.V.; Sergeev, V.P.; Neyfeld, V.V.; Popova, N.A. Features of surface layer structure of VT23 titanium alloy under bombardment with copper ions. *AIP Conf. Proc.* **2015**, *1683*. [CrossRef]
33. Ma, Z.Y. Friction Stir Processing Technology: A Review. *Metall. Mater. Trans. A* **2008**, *39*, 642–658. [CrossRef]
34. Kumar, R.A.; Kumar, R.G.A.; Ahamed, K.A.; Alstyn, B.D.; Vignesh, V. Review of Friction Stir Processing of Aluminium Alloys. *Mater. Today Proc.* **2019**, *16*, 1048–1054. [CrossRef]
35. Węglowski, M.S. Friction stir processing – State of the art. *Arch. Civ. Mech. Eng.* **2018**, *18*, 114–129. [CrossRef]
36. Padhy, G.K.; Wu, C.S.; Gao, S. Friction stir based welding and processing technologies - processes, parameters, microstructures and applications: A review. *J. Mater. Sci. Technol.* **2018**, *34*, 1–38. [CrossRef]
37. Rao, A.G.; Ravi, K.R.; Ramakrishnarao, B.; Deshmukh, V.P.; Sharma, A.; Prabhu, N.; Kashyap, B.P. Recrystallization Phenomena During Friction Stir Processing of Hypereutectic Aluminum-Silicon Alloy. *Metall. Mater. Trans. A* **2013**, *44*, 1519–1529. [CrossRef]
38. Sun, H.; Yang, S.; Jin, D. Improvement of Microstructure, Mechanical Properties and Corrosion Resistance of Cast Al–12Si Alloy by Friction Stir Processing. *Trans. Indian Inst. Met.* **2018**, *71*, 985–991. [CrossRef]
39. Zhao, H.; Pan, Q.; Qin, Q.; Wu, Y.; Su, X. Effect of the processing parameters of friction stir processing on the microstructure and mechanical properties of 6063 aluminum alloy. *Mater. Sci. Eng. A* **2019**, *751*, 70–79. [CrossRef]
40. Abrahams, R.; Mikhail, J.; Fasihi, P. Effect of friction stir process parameters on the mechanical properties of 5005-H34 and 7075-T651 aluminium alloys. *Mater. Sci. Eng. A* **2019**, *751*, 363–373. [CrossRef]
41. Kalashnikov, K.N.; Vorontsov, A.V.; Kalashnikova, T.A.; Chumaevskii, A.V. Changes in the structure and properties of aluminum alloys during friction stir processing by different types of tools. *AIP Conf. Proc.* **2018**, *2053*, 40038. [CrossRef]
42. Kalashnikov, K.N.; Tarasov, S.Y.; Chumaevskii, A.V.; Fortuna, S.V.; Eliseev, A.A.; Ivanov, A.N. Towards aging in a multipass friction stir–processed AA2024. *Int. J. Adv. Manuf. Technol.* **2019**, *103*, 2121–2132. [CrossRef]
43. Ramesh, K.N.; Pradeep, S.; Pancholi, V. Multipass Friction-Stir Processing and its Effect on Mechanical Properties of Aluminum Alloy 5086. *Metall. Mater. Trans. A* **2012**, *43*, 4311–4319. [CrossRef]

44. Senthilkumar, R.; Prakash, M.; Arun, N.; Jeyakumar, A.A. The effect of the number of passes in friction stir processing of aluminum alloy (AA6082) and its failure analysis. *Appl. Surf. Sci.* **2019**, *491*, 420–431. [CrossRef]
45. Barmouz, M.; Givi, M.K.B.; Seyfi, J. On the role of processing parameters in producing Cu/SiC metal matrix composites via friction stir processing: Investigating microstructure, microhardness, wear and tensile behavior. *Mater. Charact.* **2011**, *62*, 108–117. [CrossRef]
46. Cartigueyen, S.; Mahadevan, K. Role of Friction Stir Processing on Copper and Copper based Particle Reinforced Composites—A Review. *J. Mater. Sci. Surf. Eng.* **2015**, *2*, 133–145.
47. Surekha, K.; Els-Botes, A. Development of high strength, high conductivity copper by friction stir processing. *Mater. Des.* **2011**, *32*, 911–916. [CrossRef]
48. Wang, Y.; Fu, R.; Jing, L.; Li, Y.; Sang, D. Grain refinement and nanostructure formation in pure copper during cryogenic friction stir processing. *Mater. Sci. Eng. A* **2017**, *703*, 470–476. [CrossRef]
49. Cartigueyen, S.; Mahadevan, K. Influence of rotational speed on the formation of friction stir processed zone in pure copper at low-heat input conditions. *J. Manuf. Process.* **2015**, *18*, 124–130. [CrossRef]
50. Bheekya Naik, R.; Venkateswara Reddy, K.; Madhusudhan Reddy, G.; Arockia Kumar, R. Development of High-Strength and High-Electrical Conductivity Cu–Zr Alloy Through Friction Stir Processing. *Trans. Indian Inst. Met.* **2019**, *72*, 1431–1435. [CrossRef]
51. Jiang, L.; Huang, W.; Liu, C.; Chai, L.; Yang, X.; Xu, Q. Microstructure, texture evolution and mechanical properties of pure Ti by friction stir processing with slow rotation speed. *Mater. Charact.* **2019**, *148*, 1–8. [CrossRef]
52. Mironov, S.; Sato, Y.S.; Kokawa, H. Development of grain structure during friction stir welding of pure titanium. *Acta Mater.* **2009**, *57*, 4519–4528. [CrossRef]
53. Liu, F.C.; Liao, J.; Gao, Y.; Nakata, K. Influence of texture on strain localization in stir zone of friction stir welded titanium. *J. Alloys Compd.* **2015**, *626*, 304–308. [CrossRef]
54. Zhang, W.; Ding, H.; Cai, M.; Yang, W.; Li, J. Ultra-grain refinement and enhanced low-temperature superplasticity in a friction stir-processed Ti-6Al-4V alloy. *Mater. Sci. Eng. A* **2018**, *727*, 90–96. [CrossRef]
55. Vakili-Azghandi, M.; Roknian, M.; Szpunar, J.A.; Mousavizade, S.M. Surface modification of pure titanium via friction stir processing: Microstructure evolution and dry sliding wear performance. *J. Alloys Compd.* **2020**, *816*, 152557. [CrossRef]
56. Kalashnikov, K.N.; Kalashnikova, T.A.; Chumaevskii, A.V.; Tarasov, S.Y.; Rubtsov, V.E.; Ivanov, A.N.; Kolubaev, E.A. High-strength friction stir processed dispersion hardened Al-Cu-Mg alloy. *AIP Conf. Proc.* **2017**, *1909*, 1–5. [CrossRef]
57. Kalashnikov, K.N.; Kalashnikova, T.A.; Chumaevskii, A.V.; Ivanov, A.N.; Tarasov, S.Y.; Rubtsov, V.E.; Kolubaev, E.A. Friction-stir processed ultrafine grain high-strength Al-Mg alloy material. *AIP Conf. Proc.* **2017**, *1909*, 1–6. [CrossRef]
58. Barati, M.; Abbasi, M.; Abedini, M. The effects of friction stir processing and friction stir vibration processing on mechanical, wear and corrosion characteristics of Al6061/SiO2 surface composite. *J. Manuf. Process.* **2019**, *45*, 491–497. [CrossRef]
59. Dolatkhah, A.; Golbabaei, P.; Givi, M.K.B.; Molaiekiya, F. Investigating effects of process parameters on microstructural and mechanical properties of Al5052/SiC metal matrix composite fabricated via friction stir processing. *Mater. Des.* **2012**, *37*, 458–464. [CrossRef]
60. Huang, C.W.; Aoh, J.N. Friction stir processing of copper-coated SiC particulate-reinforced aluminum matrix composite. *Materials* **2018**, *11*, 599. [CrossRef]
61. Manochehrian, A.; Heidarpour, A.; Mazaheri, Y.; Ghasemi, S. On the surface reinforcing of A356 aluminum alloy by nanolayered Ti3AlC2 MAX phase via friction stir processing. *Surf. Coat. Technol.* **2019**, *377*, 124884. [CrossRef]
62. Jain, V.K.S.; Varghese, J.; Muthukumaran, S. Effect of First and Second Passes on Microstructure and Wear Properties of Titanium Dioxide-Reinforced Aluminum Surface Composite via Friction Stir Processing. *Arab. J. Sci. Eng.* **2019**, *44*, 949–957. [CrossRef]

63. Abraham, S.J.; Dinaharan, I.; Selvam, J.D.R.; Akinlabi, E.T. Microstructural characterization of vanadium particles reinforced AA6063 aluminum matrix composites via friction stir processing with improved tensile strength and appreciable ductility. *Compos. Commun.* **2019**, *12*, 54–58. [CrossRef]
64. Bourkhani, R.D.; Eivani, A.R.; Nateghi, H.R. Through-thickness inhomogeneity in microstructure and tensile properties and tribological performance of friction stir processed AA1050-Al2O3 nanocomposite. *Compos. Part B Eng.* **2019**, *174*, 107061. [CrossRef]
65. Zahmatkesh, B.; Enayati, M.H. A novel approach for development of surface nanocomposite by friction stir processing. *Mater. Sci. Eng. A* **2010**, *527*, 6734–6740. [CrossRef]
66. Prabhu, M.S.; Perumal, A.E.; Arulvel, S.; Issac, R.F. Friction and wear measurements of friction stir processed aluminium alloy 6082/$CaCO_3$ composite. *Measurement* **2019**, *142*, 10–20. [CrossRef]
67. Deore, H.A.; Mishra, J.; Rao, A.G.; Mehtani, H.; Hiwarkar, V.D. Effect of filler material and post process ageing treatment on microstructure, mechanical properties and wear behaviour of friction stir processed AA 7075 surface composites. *Surf. Coat. Technol.* **2019**, *374*, 52–64. [CrossRef]
68. Zhang, S.; Chen, G.; Wei, J.; Liu, Y.; Xie, R.; Liu, Q.; Zeng, S.; Zhang, G.; Shi, Q. Effects of energy input during friction stir processing on microstructures and mechanical properties of aluminum/carbon nanotubes nanocomposites. *J. Alloys Compd.* **2019**, *798*, 523–530. [CrossRef]
69. Nazari, M.; Eskandari, H.; Khodabakhshi, F. Production and characterization of an advanced AA6061-Graphene-TiB2 hybrid surface nanocomposite by multi-pass friction stir processing. *Surf. Coat. Technol.* **2019**, *377*, 124914. [CrossRef]
70. Pol, N.; Verma, G.; Pandey, R.P.; Shanmugasundaram, T. Fabrication of AA7005/TiB2-B4C surface composite by friction stir processing: Evaluation of ballistic behaviour. *Def. Technol.* **2019**, *15*, 363–368. [CrossRef]
71. Dinaharan, I.; Sathiskumar, R.; Murugan, N. Effect of ceramic particulate type on microstructure and properties of copper matrix composites synthesized by friction stir processing. *J. Mater. Res. Technol.* **2016**, *5*, 302–316. [CrossRef]
72. Heidarpour, A.; Mazaheri, Y.; Roknian, M.; Ghasemi, S. Development of Cu-TiO2 surface nanocomposite by friction stir processing: Effect of pass number on microstructure, mechanical properties, tribological and corrosion behavior. *J. Alloys Compd.* **2019**, *783*, 886–897. [CrossRef]
73. Thankachan, T.; Prakash, K.S.; Kavimani, V. Investigating the effects of hybrid reinforcement particles on the microstructural, mechanical and tribological properties of friction stir processed copper surface composites. *Compos. Part B Eng.* **2019**, *174*, 107057. [CrossRef]
74. Sharma, S.; Handa, A.; Singh, S.S.; Verma, D. Influence of tool rotation speeds on mechanical and morphological properties of friction stir processed nano hybrid composite of MWCNT-Graphene-AZ31 magnesium. *J. Magnes. Alloy.* **2019**, *7*, 487–500. [CrossRef]
75. Arokiasamy, S.; Ronald, B.A. Enhanced properties of Magnesium based metal matrix composites via Friction Stir Processing. *Mater. Today Proc.* **2018**, *5*, 6934–6939. [CrossRef]
76. Satish Kumar, T.; Suganya Priyadharshini, G.; Shalini, S.; Krishna Kumar, K.; Subramanian, R. Characterization of NbC-Reinforced AA7075 Alloy Composites Produced Using Friction Stir Processing. *Trans. Indian Inst. Met.* **2019**, *72*, 1593–1596. [CrossRef]
77. Gangil, N.; Nagar, H.; Kumar, R.; Singh, D. Shape memory alloy reinforced magnesium matrix composite fabricated via friction stir processing. *Mater. Today Proc.* **2020**. [CrossRef]
78. Adetunla, A.; Akinlabi, E. Fabrication of Aluminum Matrix Composites for Automotive Industry Via Multipass Friction Stir Processing Technique. *Int. J. Automot. Technol.* **2019**, *20*, 1079–1088. [CrossRef]
79. Fotoohi, H.; Lotfi, B.; Sadeghian, Z.; Byeon, J. Microstructural characterization and properties of in situ Al-Al3Ni/TiC hybrid composite fabricated by friction stir processing using reactive powder. *Mater. Charact.* **2019**, *149*, 124–132. [CrossRef]
80. Alidokht, S.A.; Abdollah-zadeh, A.; Soleymani, S.; Assadi, H. Microstructure and tribological performance of an aluminium alloy based hybrid composite produced by friction stir processing. *Mater. Des.* **2011**, *32*, 2727–2733. [CrossRef]
81. Dinaharan, I.; Akinlabi, E.T. Low cost metal matrix composites based on aluminum, magnesium and copper reinforced with fly ash prepared using friction stir processing. *Compos. Commun.* **2018**, *9*, 22–26. [CrossRef]

82. Azimi-Roeen, G.; Kashani-Bozorg, S.F.; Nosko, M.; Nagy, Š.; Matko, I. Correction to: Formation of Al/($Al_{13}Fe_4$ + Al_2O_3) Nano-composites via Mechanical Alloying and Friction Stir Processing. *J. Mater. Eng. Perform.* **2018**, *27*, 6800. [CrossRef]
83. Mahmoud, E.R.I.; Al-qozaim, A.M.A. Fabrication of In-Situ Al–Cu Intermetallics on Aluminum Surface by Friction Stir Processing. *Arab. J. Sci. Eng.* **2016**, *41*, 1757–1769. [CrossRef]
84. Golmohammadi, M.; Atapour, M.; Ashrafi, A. Fabrication and wear characterization of an A413/Ni surface metal matrix composite fabricated via friction stir processing. *Mater. Des.* **2015**, *85*, 471–482. [CrossRef]
85. Qian, J.; Li, J.; Xiong, J.; Zhang, F.; Lin, X. In situ synthesizing Al3Ni for fabrication of intermetallic-reinforced aluminum alloy composites by friction stir processing. *Mater. Sci. Eng. A* **2012**, *550*, 279–285. [CrossRef]
86. Zeidabadi, S.R.H.; Daneshmanesh, H. Fabrication and characterization of in-situ Al/Nb metal/intermetallic surface composite by friction stir processing. *Mater. Sci. Eng. A* **2017**, *702*, 189–195. [CrossRef]
87. Khodabakhshi, F.; Arab, S.M.; Švec, P.; Gerlich, A.P. Fabrication of a new Al-Mg/graphene nanocomposite by multi-pass friction-stir processing: Dispersion, microstructure, stability, and strengthening. *Mater. Charact.* **2017**, *132*, 92–107. [CrossRef]
88. Wang, T.; Gwalani, B.; Shukla, S.; Frank, M.; Mishra, R.S. Development of in situ composites via reactive friction stir processing of Ti–B4C system. *Compos. Part B Eng.* **2019**, *172*, 54–60. [CrossRef]
89. Khodabakhshi, F.; Rahmati, R.; Nosko, M.; Orovčík, L.; Nagy, Š.; Gerlich, A.P. Orientation structural mapping and textural characterization of a CP-Ti/HA surface nanocomposite produced by friction-stir processing. *Surf. Coat. Technol.* **2019**, *374*, 460–475. [CrossRef]
90. Kumar, H.; Prasad, R.; Kumar, P.; Tewari, S.P.; Singh, J.K. Mechanical and tribological characterization of industrial wastes reinforced aluminum alloy composites fabricated via friction stir processing. *J. Alloys Compd.* **2020**, *831*, 154832. [CrossRef]
91. Kumar, K.N.; Aravindkumar, N.; Eswaramoorthi, K. Fabrication of AA6016/(Al_2O_3 + AlN) hybrid surface composite using friction stir processing. *Mater. Today Proc.* **2020**. [CrossRef]
92. Mishra, R.S.; Ma, Z.Y. Friction stir welding and processing. *Mater. Sci. Eng. R Reports* **2005**, *50*, 1–78. [CrossRef]
93. Li, K.; Liu, X.; Zhao, Y. Research Status and Prospect of Friction Stir Processing Technology. *Coatings* **2019**, *9*, 129. [CrossRef]
94. Tarasov, S.Y.; Rubtsov, V.E.; Fortuna, S.V.; Eliseev, A.A.; Chumaevsky, A.V.; Kalashnikova, T.A.; Kolubaev, E.A. Ultrasonic-assisted aging in friction stir welding on Al-Cu-Li-Mg aluminum alloy. *Weld. World* **2017**, *61*, 679–690. [CrossRef]
95. Sathiskumar, R.; Murugan, N.; Dinaharan, I.; Vijay, S.J. Role of friction stir processing parameters on microstructure and microhardness of boron carbide particulate reinforced copper surface composites. *Sadhana* **2013**, *38*, 1433–1450. [CrossRef]
96. Chen, C.F.; Kao, P.W.; Chang, L.W.; Ho, N.J. Effect of processing parameters on microstructure and mechanical properties of an Al-Al11Ce3-Al2O3 in-situ composite produced by friction stir processing. *Metall. Mater. Trans. A Phys. Metall. Mater. Sci.* **2010**, *41*, 513–522. [CrossRef]
97. Shahi, A.; Sohi, M.H.; Ahmadkhaniha, D.; Ghambari, M. In situ formation of Al–Al3Ni composites on commercially pure aluminium by friction stir processing. *Int. J. Adv. Manuf. Technol.* **2014**, *75*, 1331–1337. [CrossRef]
98. You, G.L.; Ho, N.J.; Kao, P.W. Aluminum based in situ nanocomposite produced from Al–Mg–CuO powder mixture by using friction stir processing. *Mater. Lett.* **2013**, *100*, 219–222. [CrossRef]
99. Hsu, C.J.; Kao, P.W.; Ho, N.J. Ultrafine-grained Al–Al2Cu composite produced in situ by friction stir processing. *Scr. Mater.* **2005**, *53*, 341–345. [CrossRef]
100. Fattah-alhosseini, A.; Vakili-Azghandi, M.; Sheikhi, M.; Keshavarz, M.K. Passive and electrochemical response of friction stir processed pure Titanium. *J. Alloys Compd.* **2017**, *704*, 499–508. [CrossRef]
101. Al-Fadhalah, K.J.; Almazrouee, A.I.; Aloraier, A.S. Microstructure and mechanical properties of multi-pass friction stir processed aluminum alloy 6063. *Mater. Des.* **2014**, *53*, 550–560. [CrossRef]
102. Nakata, K.; Kim, Y.G.; Fujii, H.; Tsumura, T.; Komazaki, T. Improvement of mechanical properties of aluminum die casting alloy by multi-pass friction stir processing. *Mater. Sci. Eng. A* **2006**, *437*, 274–280. [CrossRef]

103. El-Rayes, M.M.; El-Danaf, E.A. The influence of multi-pass friction stir processing on the microstructural and mechanical properties of Aluminum Alloy 6082. *J. Mater. Process. Technol.* **2012**, *212*, 1157–1168. [CrossRef]
104. Girish, G.; Anandakrishnan, V. Determination of friction stir processing window for AA7075. *Mater. Today Proc.* **2020**, *21*, 557–562. [CrossRef]
105. Yang, R.; Zhang, Z.; Zhao, Y.; Chen, G.; Guo, Y.; Liu, M.; Zhang, J. Effect of multi-pass friction stir processing on microstructure and mechanical properties of Al3Ti/A356 composites. *Mater. Charact.* **2015**, *106*, 62–69. [CrossRef]
106. John, J.; Shanmughanatan, S.P.; Kiran, M.B. Effect of tool geometry on microstructure and mechanical Properties of friction stir processed AA2024-T351 aluminium alloy. *Mater. Today Proc.* **2018**, *5*, 2965–2979. [CrossRef]
107. Cartigueyen, S.; Mahadevan, K. Study of friction stir processed zone under different tool pin profiles in pure copper. *IOSR J. Mech. Civ. Eng.* **2014**, *11*, 6–12. [CrossRef]
108. Vijayavel, P.; Balasubramanian, V. Effect of pin profile volume ratio on microstructure and tensile properties of friction stir processed aluminum based metal matrix composites. *J. Alloys Compd.* **2017**, *729*, 828–842. [CrossRef]
109. Surekha, K.; Murty, B.S.; Rao, K.P. Microstructural characterization and corrosion behavior of multipass friction stir processed AA2219 aluminium alloy. *Surf. Coat. Technol.* **2008**, *202*, 4057–4068. [CrossRef]
110. Barmouz, M.; Besharati Givi, M.K.; Jafari, J. Evaluation of Tensile Deformation Properties of Friction Stir Processed Pure Copper: Effect of Processing Parameters and Pass Number. *J. Mater. Eng. Perform.* **2014**, *23*, 101–107. [CrossRef]
111. Luo, P.; McDonald, D.T.; Xu, W.; Palanisamy, S.; Dargusch, M.S.; Xia, K. A modified Hall–Petch relationship in ultrafine-grained titanium recycled from chips by equal channel angular pressing. *Scr. Mater.* **2012**, *66*, 785–788. [CrossRef]
112. Besharati Givi, M.K.; Asadi, P.; Bag, S.; Yaduwanshi, D.; Pal, S.; Heidarzadeh, A.; Mudani, S.; Kazemi-Choobi, K.; Hanifian, H.; Braga, D.; et al. *Advances in Friction-Stir Welding and Processing*; Elsevier: Amsterdam, The Netherlands, 2014; ISBN 9780857094544.
113. Babu, J.; Anjaiah, M.; Mathew, A. Experimental studies on Friction stir processing of AZ31 Magnesium alloy. *Mater. Today Proc.* **2018**, *5*, 4515–4522. [CrossRef]
114. Pan, L.; Kwok, C.T.; Lo, K.H. Friction-stir processing of AISI 440C high-carbon martensitic stainless steel for improving hardness and corrosion resistance. *J. Mater. Process. Technol.* **2020**, *277*, 116448. [CrossRef]
115. Lashgari, H.R.; Kong, C.; Asnavandi, M.; Zangeneh, S. The effect of friction stir processing (FSP) on the microstructure, nanomechanical and corrosion properties of low carbon CoCr28Mo5 alloy. *Surf. Coat. Technol.* **2018**, *354*, 390–404. [CrossRef]
116. Jiang, X.; Overman, N.; Canfield, N.; Ross, K. Friction stir processing of dual certified 304/304L austenitic stainless steel for improved cavitation erosion resistance. *Appl. Surf. Sci.* **2019**, *471*, 387–393. [CrossRef]
117. Grewal, H.S.; Arora, H.S.; Singh, H.; Agrawal, A. Surface modification of hydroturbine steel using friction stir processing. *Appl. Surf. Sci.* **2013**, *268*, 547–555. [CrossRef]
118. Yasavol, N.; Jafari, H. Microstructure, Mechanical and Corrosion Properties of Friction Stir-Processed AISI D2 Tool Steel. *J. Mater. Eng. Perform.* **2015**, *24*, 2151–2157. [CrossRef]
119. Singh, S.; Kaur, M.; Saravanan, I. Enhanced microstructure and mechanical properties of boiler steel via Friction Stir Processing. *Mater. Today Proc.* **2020**, *22*, 482–486. [CrossRef]
120. Wang, T.; Shukla, S.; Komarasamy, M.; Liu, K.; Mishra, R.S. Towards heterogeneous AlxCoCrFeNi high entropy alloy via friction stir processing. *Mater. Lett.* **2019**, *236*, 472–475. [CrossRef]
121. Yang, X.; Yan, Z.; Dong, P.; Cheng, B.; Zhang, J.; Zhang, T.; Zhang, H.; Wang, W. Surface modification of aluminum alloy by incorporation of AlCoCrFeNi high entropy alloy particles via underwater friction stir processing. *Surf. Coat. Technol.* **2020**, *385*, 125438. [CrossRef]
122. Wang, T.; Komarasamy, M.; Shukla, S.; Mishra, R.S. Simultaneous enhancement of strength and ductility in an AlCoCrFeNi2.1 eutectic high-entropy alloy via friction stir processing. *J. Alloys Compd.* **2018**, *766*, 312–317. [CrossRef]

123. Yang, X.; Dong, P.; Yan, Z.; Cheng, B.; Zhai, X.; Chen, H.; Zhang, H.; Wang, W. AlCoCrFeNi high-entropy alloy particle reinforced 5083Al matrix composites with fine grain structure fabricated by submerged friction stir processing. *J. Alloys Compd.* **2020**, *836*, 155411. [CrossRef]
124. Sinha, S.; Nene, S.S.; Frank, M.; Liu, K.; Lebensohn, R.A.; Mishra, R.S. Deformation mechanisms and ductile fracture characteristics of a friction stir processed transformative high entropy alloy. *Acta Mater.* **2020**, *184*, 164–178. [CrossRef]
125. Shukla, S.; Wang, T.; Frank, M.; Agrawal, P.; Sinha, S.; Mirshams, R.A.; Mishra, R.S. Friction stir gradient alloying: A novel solid-state high throughput screening technique for high entropy alloys. *Mater. Today Commun.* **2020**, *23*, 100869. [CrossRef]
126. Leal, R.M.; Galvão, I.; Loureiro, A.; Rodrigues, D.M. Effect of friction stir processing parameters on the microstructural and electrical properties of copper. *Int. J. Adv. Manuf. Technol.* **2015**, *80*, 1655–1663. [CrossRef]
127. Peng, J.; Zhang, Z.; Huang, J.; Guo, P.; Li, Y.; Zhou, W.; Wu, Y. The effect of the inhomogeneous microstructure and texture on the mechanical properties of AZ31 Mg alloys processed by friction stir processing. *J. Alloys Compd.* **2019**, *792*, 16–24. [CrossRef]
128. Wang, Y.; Huang, Y.; Meng, X.; Wan, L.; Feng, J. Microstructural evolution and mechanical properties of MgZnYZr alloy during friction stir processing. *J. Alloys Compd.* **2017**, *696*, 875–883. [CrossRef]
129. Shang, Q.; Ni, D.R.; Xue, P.; Xiao, B.L.; Wang, K.S.; Ma, Z.Y. An approach to enhancement of Mg alloy joint performance by additional pass of friction stir processing. *J. Mater. Process. Technol.* **2019**, *264*, 336–345. [CrossRef]
130. Du, X.; Wu, B. Using two-pass friction stir processing to produce nanocrystalline microstructure in AZ61 magnesium alloy. *Sci. China Ser. E Technol. Sci.* **2009**, *52*, 1751–1755. [CrossRef]
131. Huang, L.; Wang, K.; Wang, W.; Yuan, J.; Qiao, K.; Yang, T.; Peng, P.; Li, T. Effects of grain size and texture on stress corrosion cracking of friction stir processed AZ80 magnesium alloy. *Eng. Fail. Anal.* **2018**, *92*, 392–404. [CrossRef]
132. Jin, Y.; Wang, K.; Wang, W.; Peng, P.; Zhou, S.; Huang, L.; Yang, T.; Qiao, K.; Zhang, B.; Cai, J.; et al. Microstructure and mechanical properties of AE42 rare earth-containing magnesium alloy prepared by friction stir processing. *Mater. Charact.* **2019**, *150*, 52–61. [CrossRef]
133. MD, F.K.; Karthik, G.M.; Panigrahi, S.K.; Ram, G.D.J. Friction stir processing of QE22 magnesium alloy to achieve ultrafine-grained microstructure with enhanced room temperature ductility and texture weakening. *Mater. Charact.* **2019**, *147*, 365–378. [CrossRef]
134. Johannes, L.B.; Yowell, L.L.; Sosa, E.; Arepalli, S.; Mishra, R.S. Survivability of single-walled carbon nanotubes during friction stir processing. *Nanotechnology* **2006**, *17*, 3081–3084. [CrossRef]
135. Reddy, K.V.; Naik, R.B.; Rao, G.R.; Reddy, G.M.; Kumar, R.A. Microstructure and damping capacity of AA6061/graphite surface composites produced through friction stir processing. *Compos. Commun.* **2020**, *20*, 100352. [CrossRef]
136. Kumar, P.A.; Madhu, H.C.; Pariyar, A.; Perugu, C.S.; Kailas, S.V.; Garg, U.; Rohatgi, P. Friction stir processing of squeeze cast A356 with surface compacted graphene nanoplatelets (GNPs) for the synthesis of metal matrix composites. *Mater. Sci. Eng. A* **2020**, *769*, 138517. [CrossRef]
137. Mishra, R.S.; Ma, Z.Y.; Charit, I. Friction stir processing: A novel technique for fabrication of surface composite. *Mater. Sci. Eng. A* **2003**, *341*, 307–310. [CrossRef]
138. Khorrami, M.S.; Saito, N.; Miyashita, Y.; Kondo, M. Texture variations and mechanical properties of aluminum during severe plastic deformation and friction stir processing with SiC nanoparticles. *Mater. Sci. Eng. A* **2019**, *744*, 349–364. [CrossRef]
139. Sivanesh Prabhu, M.; Elaya Perumal, A.; Arulvel, S. Development of multi-pass processed AA6082/SiCp surface composite using friction stir processing and its mechanical and tribology characterization. *Surf. Coat. Technol.* **2020**, *394*, 125900. [CrossRef]
140. Shamsipur, A.; Kashani-Bozorg, S.F.; Zarei-Hanzaki, A. The effects of friction-stir process parameters on the fabrication of Ti/SiC nano-composite surface layer. *Surf. Coat. Technol.* **2011**, *206*, 1372–1381. [CrossRef]
141. Shafiei-Zarghani, A.; Kashani-Bozorg, S.F.; Gerlich, A.P. Texture Analyses of Ti/Al2O3 Nanocomposite Produced Using Friction Stir Processing. *Metall. Mater. Trans. A Phys. Metall. Mater. Sci.* **2016**, *47*, 5618–5629. [CrossRef]

142. Shang, J.; Ke, L.; Liu, F.; Lv, F.; Xing, L. Aging behavior of nano SiC particles reinforced AZ91D composite fabricated via friction stir processing. *J. Alloys Compd.* **2019**, *797*, 1240–1248. [CrossRef]
143. Zhang, Q.; Xiao, B.L.; Wang, Q.Z.; Ma, Z.Y. In situ Al3Ti and Al2O3 nanoparticles reinforced Al composites produced by friction stir processing in an Al-TiO2 system. *Mater. Lett.* **2011**, *65*, 2070–2072. [CrossRef]
144. Dixit, S.; Mahata, A.; Mahapatra, D.R.; Kailas, S.V.; Chattopadhyay, K. Multi-layer graphene reinforced aluminum – Manufacturing of high strength composite by friction stir alloying. *Compos. Part B Eng.* **2018**, *136*, 63–71. [CrossRef]